University of Bath

MSC

Stabilising and Validating the Met Office's Unified Model with 100 and 120 km ceilings

Harry, Gabriel

Award date:
2014

Awarding institution:
University of Bath

Link to publication

Alternative formats
If you require this document in an alternative format, please contact:
openaccess@bath.ac.uk

Copyright of this thesis rests with the author. Access is subject to the above licence, if given. If no licence is specified above, original content in this thesis is licensed under the terms of the Creative Commons Attribution-NonCommercial 4.0 International (CC BY-NC-ND 4.0) Licence (https://creativecommons.org/licenses/by-nc-nd/4.0/). Any third-party copyright material present remains the property of its respective owner(s) and is licensed under its existing terms.

Take down policy
If you consider content within Bath's Research Portal to be in breach of UK law, please contact: openaccess@bath.ac.uk with the details. Your claim will be investigated and, where appropriate, the item will be removed from public view as soon as possible.

Download date: 05. May. 2023

Stabilising and Validating the Met Office's Unified Model with 100 and 120 km Ceilings

by

Gabriel Harry

Thesis presented to the University of Bath in partial fulfillment of MSc Modern Applications of Mathematics

Declaration

I hereby declare that I am the sole author of this thesis, except where references are indicated. This is a true copy of the thesis, including any required final revisions.

December 2014

Abstract

The Met Office is a globally recognised organisation in the field of numerical weather prediction and weather and climate science, with its forecasting services consistently ranked as one of the top two in the world. It maintains this standing via continuous refinements, improvements and upgrades to its operations and computer models. One frontier it is currently exploring is space weather, having opened a dedicated operational centre in October 2014. Space weather impacts the high atmosphere and can affect technological systems onboard spacecraft, as well as GPS and radio communications. In order to model space weather, the Met Office is beginning to implement raised altitudes within its simulation of the atmosphere - far higher than is currently used to model accurately everyday weather systems closer to the ground, with its current weather and climate systems simulating an atmosphere that is 80 km deep.

This project is concerned with extension of the model's upper boundary, first to 100 km in altitude, then to 120 km, with a focus on the stability and validity of the simulations. The method I used for stabilising the runs was, initially, altering various setup parameters (namely, timestep, resubmission pattern, α, and the vertical damping coefficient), logging these alterations, running the simulation, and logging the amount of time the simulation runs before crashing. I then implemented slightly different alterations and compared their effects on stability to the previous alterations, and continued this process. The results are validated by comparing the state of a given variable within the simulated atmosphere with its equivalent state in observed data, namely temperature data taken from NASA's Microwave Limb Sounder (MLS) instrument aboard the Aura satellite, and wind data from the UARS Reference Atmosphere Project (URAP).

Assessment of the UM with a 100 km upper boundary showed good representation of air temperature, albeit with a notably colder winter mesospheric south pole, but some misrepresentation of jet structure and speed. Attempts were made to run the UM with an upper boundary of 120 km, where improved stability was noted when a high off-centring parameter and a discovered "sweet spot" value of the vertical damping coefficient was chosen. The non-orographic gravity wave scheme was revealed to be a significant beneficiary to model realism, namely wind speed and south pole mesospheric winter temperatures. Rayleigh damping code for the u and v directions was successfully implemented for compiling and submitting to the supercomputer, however this code did not run past the first timestep.

Useful discoveries were made in this project, particularly with the discovery of noteworthy activity at the simulated atmosphere's north and south poles, analysis of the effect of the non-orographic gravity wave scheme, and the discovery of an effective vertical damping value - the latter resulting in a UM run with the highest recorded 120 km upper boundary stability thus far. The work done in this project should prove valuable in the Met Office's objectives regarding the improvement of the Unified Model with heightened upper boundaries.

Acknowledgements

Thank you to David Jackson and Sophie Murray for all their help and generosity. Thank you to Corwin Wright for providing such vital data. Thank you to Edmund Henley for all the help with Python, and thank you to Tom Melvin for his expertise in implementing the Rayleigh damping. Thank you to everyone else at the Met Office for giving their time to lend me a hand, in particular Andrew Bushell, Martin McMillan, Dan Griffin and John Thuburn. And thank you to Chris Budd for giving me the privilege to work in such an inspiring place.

Contents

List of Figures

List of Tables

Nomenclature

COSPAR - The Committee on Space Research

ENDGame - Even Newer Dynamics for General Atmospheric Modelling of the Environment

GAIA - Ground-to-topside model of Atmosphere and Ionosphere for Aeronomy

GPS - Global Positioning System

LTE - Local Thermodynamic Equilibrium

MLS - Microwave Limb Sounder

SISL - Semi-implicit semi-Lagrangian

SSW - Sudden Stratospheric Warming

TEC - Total Electron Content

TIEGCM - Thermosphere-Ionosphere- Electrodynamics General Circulation Model

UARS - Upper Atmosphere Research Satellite

UM - Unified Model

UMUI - Unified Model User Interface

URAP - UARS Reference Atmosphere Project

USSP - Ultra-Simple Spectral Parameterisation

WACCM - Whole Atmosphere Community Climate Model

WAM - Whole Atmosphere Model

Chapter 1

Background

The Met Office is the UK's national weather service. It has developed from a ship-safeguarding gale forecasting service to its current state as consistently one of the top two operational weather forecasting services in the world. It offers many products outside of the weather forecast for which it is most well known. Via the Hadley Centre, the Met Office performs long term climate change research, which assists in the work of international environment agencies, aid agencies and emergency planners, as well as providing scientific advice to political bodies. In collaboration with other agencies, it provides warnings on national hazards, such as flooding and volcanic ash, the latter benefitting aviation in particular. Further to this, the Met Office provides a significant benefit to aviation organisations by producing four global wind forecasts a day, which aeroplanes can use to save fuel. It is estimated that this service saves twenty million tonnes of carbon dioxide emissions per year. The Met Office provides many other services to military, transport and industrial organisations.

The Met Office has been at the forefront of numerical weather prediction thanks to its continually improving computing power (see Table 1.1), which allows for increasingly accurate simulations of the atmosphere; the Met Office's first computer simulated an atmosphere horizontally discretised into a grid, with each grid box 320 km in length, applied to the local UK region. As of 2014, this length has shrunk to 1.5 km.

Table 1.1: History of the Met Office's computing power

Year	Computer	Calculations per second	Horizontal resolution (global/local)	Number of vertical levels
1959	Ferranti Mercury	3Kflops	N.A./320km	2
1965	English Electric KDF9	50Kflops	N.A./300km	3
1972	IBM System 360/195	4Mflops	300km/100km	10
1982	CDC Cyber 205	200Mflops	150km/75km	15
1991	Cray Y-MP C90/16	10Gflops	90km/17km	19
1997	Cray T3E 900/1200	430Gflops	60km/12km	38
2004	NEC SX-6	2.0Tflops	40km/12km	50
2006	NEC SX-8 and SX-6	5.4Tflops	40km/4km	50
2009	IBM Power6	140Tflops	17km/1.5km	70
2015	Cray XC40	16Pflops	1.5km	

This accuracy has also increased vertically, in terms of resolution and altitude. The Met Office's current simulation has 70 vertical levels, modelling the first 85 km of the atmosphere.

Further to the Met Office's national hazard warnings, it also provides space weather forecasts and and warnings. A long-term research goal is the development of a coupled, data-driven Sun-to-Earth model for enhanced space weather forecast capability. A key element of this model would be a whole atmosphere model which extends from the surface up to top of the thermosphere - this is the motivation of this project.

The project was conducted in 2014 from July to December, supervised by Prof. David Jackson and Dr. Sophie Murray. It was focused on raising the ceiling of the Met Office's Unified Model (UM) to 100 km and 120 km, incorporating 88 and 91 vertical levels respectively, and the stability and validity issues that this involves.

Chapter 2

Introduction and theory

The aims for this project were to improve the stability of the Met Office's current global atmosphere model, the UM, and assess its agreement with observations, with a heightened upper boundary. These actions were first done with the UM extended to 100 km altitude, then to 120 km. The Met Office's motivation for extending the UM's ceiling to produce a coupled Sun-to-Earth model is to model more accurately the thermosphere and its significant influence on several phenomena which are becoming increasingly relevant to human technological systems.

A common idea of the Earth's atmosphere is that it is covered by a very thin layer of atmosphere, whose proportion relative to the Earth is akin to the layer of varnish over the surface of a bowling ball (Gore, 2004). Although this illustrates the troposphere, the region of the atmosphere we experience every day, one characterised by mass, warmth and considerable weather phenomena, it overlooks an atmosphere of soaring height which, while quickly decreasing in mass and pressure, nonetheless features a host of dynamic processes, and is becoming increasingly significant to human activities. Its impacts on technology and infrastructure are set to increase, and so demand is rising for services which can model its state and effects. The Met Office is an organisation which endeavours to do so.

An early example of a comprehensive model of the atmosphere is the COSPAR International Reference Atmosphere (CIRA), an empirical model of the whole atmosphere created by the Commitee on Space Research. First created in 1961, the model features datasets containing averages for temperature, altitude, zonal velocity and pressure. The model covers north to south pole, and altitudes from 0 to 120 km, and the data has been gathered from ground-based, satellite, and radiosonde instruments. A significant use of CIRA has been to assist in planning spaceflight missions (Bilitza, 2006). While the model accurately represents significant features of the high atmosphere, as well as its broad defining structure, CIRA represents a climatology, and has no reactive capacities. There are currently many models which model a global atmosphere, with a focus on the ionosphere,

which has a particularly significant influence on human technology. However, there are a limited number which can model the whole atmosphere, and the ionosphere's shape and characteristics within it.

Upper and middle atmosphere dynamics sometimes have direct effects on weather in the troposphere, such as in weakening of western winter winds during the minimum of the Sun's 11-year sunspot cycle (Ineson et al., 2011). However, the motivation to model higher altitudes is mainly to ascertain what effects they will have on human technological systems, eg. the Global Positioning System.

Beyond this chapter, Chapter 3 will describe the UM's dynamical core, ENDGame (Even Newer Dynamics for General Atmospheric Modelling of the Environment (Walters et al., 2014)), and how it compares with those from contemporary whole atmosphere models. Chapter 4 will describe, and detail the results of, the experiments which were conducted to improve ENDGame's stability at 100 km and 120 km altitude. Chapter 5 will assess the model's validity at these altitudes, by comparing its output with satellite observations. Chapter 6 will draw conclusions from these results and suggest directions for future work.

In this chapter, the atmosphere's characteristics are described up until 120 km. At these altitudes, the atmosphere begins to blend with outer space. Its effects are therefore described as "space weather" - these are also described, along with their impacts on human technological systems.

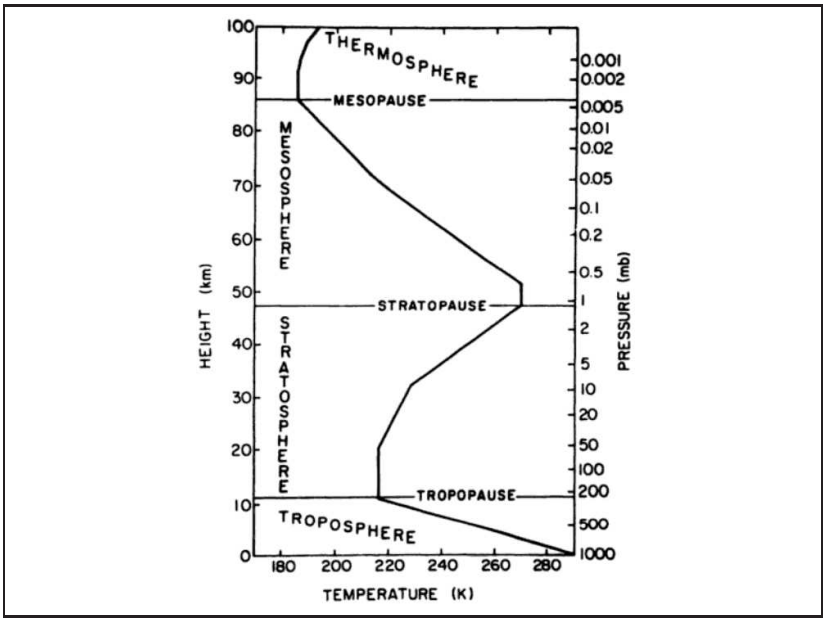

Figure 2.1: Mid-latitude temperature profile (Andrews et al., 1987)

2.1 Atmospheric layers

The atmosphere of the Earth is a layer of gases which the planet retains via gravitational attraction. It plays a crucial role in the Earth's biosphere with its capacity to regulate temperature, protect against solar radiation, and help to maintain a breathable chemical composition. The atmospheric pressure at the Earth's surface (sea level) is constant, but reduces with altitude at an exponential rate (Jacobson, 2005). The atmospheric temperature, on the other hand, has a more complicated profile as altitude increases, alternating between decreasing and increasing (see Figure 2.1). It is these temperature profiles which define the atmosphere's primary layers. Herein, these primary layers are described up until the thermosphere, representing the region of the atmosphere in which we are most interested.

1.1.1.1 Troposphere

For the first layer of the atmosphere, the primary heating mechanism is through surface radiation from below. Thus, the temperature decreases with altitude - it is this characterisation which defines the troposphere. A decreasing temperature profile continues until approximately 12km up, where there exists a relatively stable temperature boundary layer called the tropopause. Approximately 80% of the whole atmosphere's total mass is contained within the troposphere (McGraw-Hill, 1984). The surface radiation which heats the troposphere is conducive to vertical mixing and rising air currents, making the troposphere the layer which contains the majority of the atmosphere's weather activity.

1.1.1.2 Stratosphere

The stratosphere extends from the tropopause to approximately 50 km in altitude. In contrast with the troposphere, temperature increases with altitude - this is due to the layer's abundance of ozone, which absorbs solar ultraviolet radiation. The stratosphere is bounded above by the stratopause, whose height can vary with latitude and season, where a temperature maximum occurs. The stratosphere is almost completely free of clouds, air turbulence or other significant weather systems, owing to its steadily increasing temperature, which rises from 210 K (- 60 °C) at the tropopause to 270 K (- 3 °C) at the stratopause.

1.1.1.3 Mesosphere

In the mesosphere, temperature decreases with height. At its upper boundary, the mesopause, the temperature plunges to 130 K (- 143 °C), the coldest point in the Earth's atmosphere. The mesopause, similar to the aforementioned stratopause, experiences latitudinal and seasonal variations in its altitude. The layer is host to noctilucent clouds, as well as several wave processes (see section 1.2), which have been excited in the troposphere and lower stratosphere, and have propagated up to this layer. The mesosphere also contains the lower layer of the ionosphere, a region of the upper atmosphere which experiences ionisation due to solar radiation. The mesosphere extends to approximately 80 - 85 km above sea level.

1.1.1.4 Thermosphere

The thermosphere is gigantic relative to the layers below it, starting from the aforementioned mesopause at 80 - 85 km altitude and soaring to between 500 and 1000 km above sea level. The reason for its dramatic height variability is attributed to solar activity, namely geomagnetic storms (caused by coronal mass ejections[1]) and solar flares[2], which can alter the air's density and movement (Sutton, 2008). The pressure within the thermosphere is very low, exhibiting a mean free path[3] of 1 km (Ahrens & Donald, 2005). Incidentally, this means that while the temperature of each molecule may exceed 1773 K (1500 °C), any object in the thermosphere wouldn't experience extreme heat due to the severely reduced atmospheric heat transfer rate. This very low density causes radiative and chemical heating to produce an inverted temperature profile, where temperature increases with height. The thermosphere contains the anacoustic zone, which starts to take effect at approximately 160 km altitude, wherein the air pressure becomes too low for the propagation of sound waves within the normal hearing range (Darling, 2003). However, acoustic waves outside our hearing range continue to propagate into the thermosphere. Near the Earth's surface, air is mainly composed of 80% nitrogen molecules (N_2) and 20% oxygen molecules (O_2), with this composition mostly constant due to vertical atmospheric mixing - however, due to energetic photons in the X-ray and UV range breaking these molecules

[1] Coronal mass ejection: expulsions of large amounts of plasma emitted by the Sun, generally originating from solar active regions, which take one or two days to reach Earth.

[2] Solar flare: large ejection of a cloud of ions, electrons and atoms from the Sun, whose whole-spectrum electromagnetic radiation takes 8 minutes to reach Earth. Their particles take tens of minutes.

[3] Mean free path: average distance travelled by a moving particle between successive collisions.

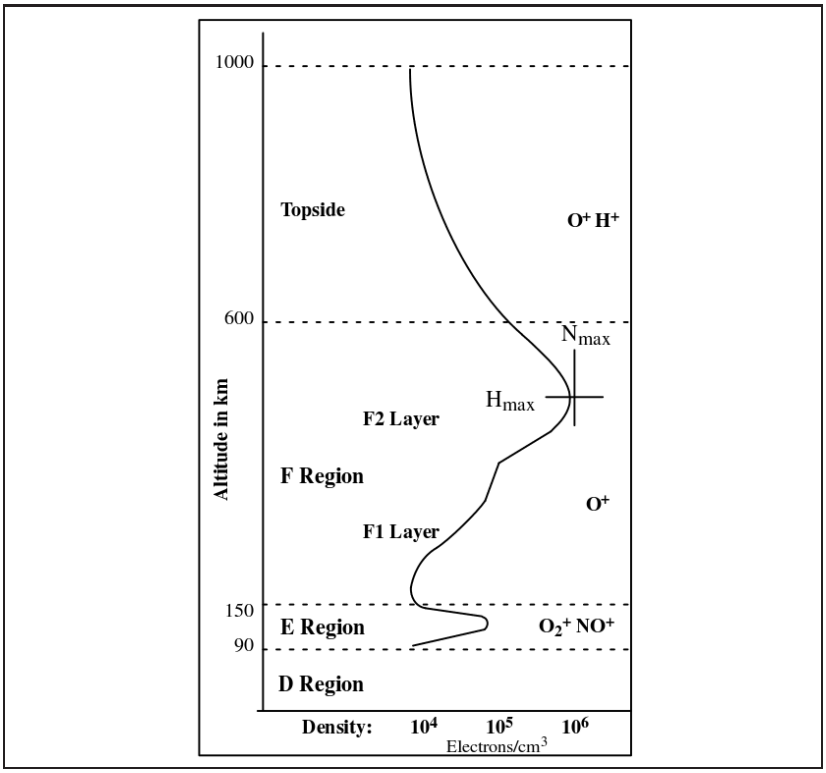

Figure 2.2: Ionospheric layers, with altitudes and predominant ion species, plotted in terms of electron density. N_{max} and H_{max} refer to the ionosphere's maximum electron density and the height at which this density occurs, repectively (Anderson & Fuller-Rowell, 1999).

apart in higher altitudes, the upper thermosphere is composed of atomic oxygen (O), atomic nitrogen (N), and helium (He). Molecular nitrogen is also present in the thermosphere, and its concentration relative to oxygen is an important feature of the thermosphere, discussed in Section 3.1.3.

2.2 Dynamics

2.2.1 Ionosphere

The ionosphere is mostly contained within the thermosphere, but its variability is significant and can extend from the upper limit of the mesosphere to beyond the thermosphere. It forms the inner region of the magnetosphere, the magnetic field of the Earth, which can extend millions of kilometres into outer space. Within the ionosphere, the altitude is such that extreme ultraviolet and x-ray photons emitted by the Sun have enough energy to ionise the normally neutral atmosphere, producing a plasma (a medium of charged ions; Kelley, 1989).

The ionosphere's two innermost layers lie within the altitudes simulated by the Met Office's models (see Figure 2.2), while

the top layer extends beyond. The D region, 60 to 90 km in altitude, draws ionisation from ultraviolet radiation (121.5 nm wavelength), which ionises nitric oxide (NO), and hard X-rays ($<$ 1nm wavelength) which, given high solar activity, may ionise N_2 and O_2. Further up, the E region, from 90 to 120 km, draws its ionisation from soft x-rays (1-10 nm wavelength) which ionise O_2. The top layer, the F region, is the most electron-dense layer. The F-region features lighter ions such as hydrogen and helium, and is responsible for the majority of reflected radio waves from ground-based communications (see section 1.2.3).

Because the ionosphere is primarily dependent on sunlight, it experiences diurnal variations as well as clear seasonal variations. In particular, its influence from solar activity is due to geomagnetic storms and charged particles, which can increase ionospheric ionisation. The ionosphere and the thermosphere vary together due to gravity waves, planetary waves and tides (see 1.2.2), which have direct and indirect effects on the F region. These wave effects are more pronounced at low latitudes, due to the E region dynamo process. This is a phenomenon where the E region is forced upwards by wave effects, thus forcing its plasma to move along geomagnetic field lines in the magnetosphere, generating an eastward electric field in the dayside, in the same mechanism as an electric dynamo along a magnet. These fields are transmitted upward along magnetic field lines into the F-region, causing the plasma to drift upward at the magnetic equator (Immel et al., 2006). The atmospheric waves are damped significantly below the peak in ionospheric density so it is counterintuitive to think they could affect electron densities in the ionosphere, however the E region dynamo effect is conducive to this. Pedatella and Forbes used the total electron content (TEC)[4] of GPS to study the coupling of the sudden stratospheric warming (SSW)[5] of 2009 with perturbations in the ionosphere, and found that zonal winds which occur during an SSW play an important role in this coupling (Forbes and Pedatella, 2010). These phenomena require attention in the Met Office's models if the ionosphere, and its impacts, are to be adequately forecast.

2.2.2 Wave phenomena

A number of wave phenomena are observed in the mesosphere and the thermosphere. The three most significant wave types are detailed here, although in reality there are several other types, including hybrids such as Rossby-gravity waves (Nappo, 2002). Due to the atmosphere's exponentially decreasing density, wave amplitudes increase exponentially with vertical propagation.

1.2.2.1 Gravity waves

Gravity waves are triggered by an initial vertical displacement of air - the main causes of this are relatively steep topographic gradients such as mountains (see Figure 2.3), and updrafts from storms. Wave motion is generated by the buoyancy force which is experienced by an air parcel displaced from its equilibrium in a stratified atmosphere such as Earth's. Upward motion

[4] Total electron content (TEC): a characteristic quantity of the ionosphere, denoting the number of electrons within a vertical column of a square metre cross sectional area. TEC is a function of solar radiation, with free electrons in the ionosphere on the night side of the Earth allowed to recombine with the ions, thus driving a daily cycle of ionospheric TEC.

[5] Sudden stratospheric warming: rapid warming (perhaps as quick as 50°C in a couple of days) in the stratosphere, caused by weakening or reversing of the Polar Night Jet, a jet stream which carries cold air during winter months.

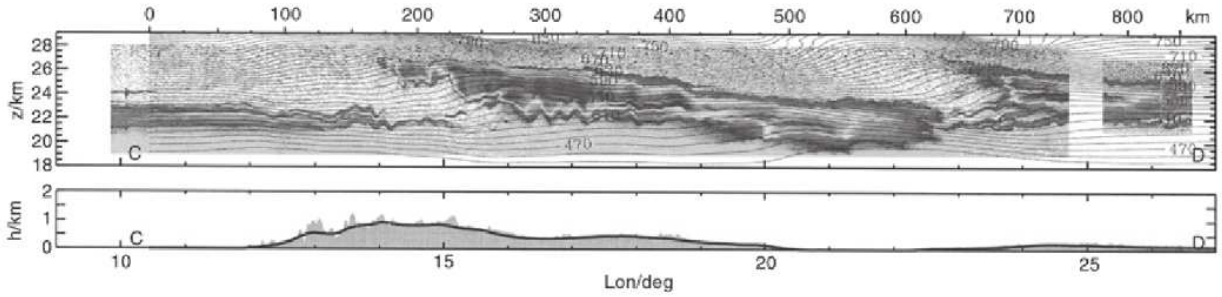

Figure 2.3: Top: observed gravity wave over Scandinavian mountain range, 26th of January 2001. Bottom: smoothed domain profile beneath wave flight track (Nappo, 2002).

is conducive to cloud formation, while downward motion causes clouds to dissipate - this can create a visible cloud ripple effect in the sky. Gravity waves are common in the upper mesosphere, where their effects can be detected by a variety of instruments, including radar (Andrews et al, 1987). Gravity waves propagate with great variety and complexity, exhibiting behaviours such as moving upward with increasing frequency and magnitude, being reflected downward, or being broken apart into smaller waves (Nappo, 2002). Gravity waves must be taken into account when modelling the high atmosphere; as Espy et al explain:

"Although gravity waves have spatial scales of only ten to a few hundred kilometers, and their temporal scales are between five minutes and several hours, they play a major role in the global dynamics, circulation and thermal balance of the mesosphere and lower thermosphere. Typically generated in the lower atmosphere through the action of weather systems or orographic lifting of air masses, the waves grow in amplitude as they propagate upward into the rarified mesosphere. There, depending upon the filtering action of the winds below, the waves can either accelerate or decelerate the mesospheric wind jets as they become unstable and locally dissipate their energy and momentum." (Espy et al., 2004)

This acceleration and deceleration must be accounted for by the Met Office's model to ensure accurate modelling of atmospheric dynamics (see Chapter 5.

1.2.2.2 Planetary waves

On a larger scale than gravity waves, planetary, or Rossby, waves exhibit periods of tens to hundreds of days. They are more limited in altitude than gravity waves, generally peaking in the stratosphere. They form due to the Coriolis force[6], combined with atmospheric air flow over mountains and other topographic regions.

In the northern hemisphere, air that is forced to ascend by flowing over a mountain or a similar object holds a tendency to turn to the right, and conversely as it descends it tends to turn to the left. This satisfies the Conservation of Absolute Vorticity, formulated by Carl-Gustav Rossby and collaborators (Rossby et al., 1939). This tendency produces a peak-trough pattern which generates waves in westerly winds. Rossby waves always have a westerly component in their phase velocities[7] - for this reason it

[6] Coriolis force: an artifact of the Earth's rotation in which air moving, say, along a pressure gradient (from high to low pressure), experiences an apparent path deflection due to the Earth's rotation. Responsible for cyclones (in the nothern hemisphere) and anti-cyclones (southern hemisphere).

[7] Phase velocity: rate at which the phase of a wave propagates through space.

is common for the Rocky Mountains and the Andes, for example, to produce Rossby waves due to their orthogonal orientation to westerlies.

1.2.2.3 Tidal waves

Unlike planetary or gravity waves, tidal waves aren't caused by the displacement of air due to terrestrial or atmospheric phenomena, but rather periodic conditions externally imposed on the atmosphere, such as the day/night effects of solar heating, and the gravitational pull of the moon (and, to a lesser degree, the Sun). They can also be excited by nonlinear interactions between aforementioned planetary waves.

The tides with the largest amplitudes have periods of 12 and 24 hours, due to their excitation by solar heating. Solar tides fall into the category of migrating and non-migrating: migrating tides propagate westwards along with the apparent motion of the Sun, while non-migrating tides propagate in a variety of directions, due to surface interactions such as topographic differences and tropical convection. Gravitational tides are much less significant than solar ones, and are caused by the moon's gravitational pull on the oceans and subsequent effects, as well as the moon and the Sun's direct gravitational influence on the atmosphere itself.

Both migrating and non-migrating tides are coupled with the dynamics of the ionosphere and can induce significant daily or weekly variability. Recently discovered is a longitudinal variation of the ionosphere on the scale of thousands of kilometres, which have been linked with non-migrating tides originating from rainstorms in the tropics (Immel et al., 2006).

2.2.3 Impacts on technology

There are a variety of impacts from high atmosphere dynamics experienced by human technological systems, which the Met Office's models can forecast. Such forecasts are valuable in their ability to increase the efficacy of these systems, save them from damage and even save lives.

Radio waves used for communication are useful because they do not need direct line of sight from sender and receiver, with their long wavelengths useful for propagation over hundreds of kilometres of terrain. Radio waves may reflect off the ionosphere and the ground many times during propagation. The most frequent mechanism for this reflection is for the direction of high-frequency (30 MHz) radio waves to be bent towards the horizontal as they propagate upwards, experiencing a decrease in the ionosphere's refractive index along with increasing altitude (Hargreaves & Hunsucker, 2003). Depending on the conditions of the ionosphere and the frequency of the wave, radio signals can be sent thousands of kilometres via this mechanism. The aforementioned E layer of the ionosphere rises at sunset, when sunlight is only incident at higher altitudes, thus benefiting radio wave propagation in reflecting from a higher F region.

Another impact of the ionosphere is experienced with GPS, which is relied upon by thousands worldwide, sometimes in life

or death situations. The ionosphere is cited to be the most significant source of error within GPS positioning and navigation. Under particular circumstances it can even cause loss of carrier signal altogether (Klobuchar, 1991). GPS radio waves exhibit higher frequencies than aforementioned ground-based radio communications and so, rather than reflect off the ionosphere while travelling from the satellite to the receiver, the signal passes down through the layer. The speed of the signal is increased with TEC, making TEC a variable to be modelled and forecast. While TEC largely varies with ionospheric exposure to solar activity, it can also change rapidly, sometimes on the order of 10 minutes. These rapid changes are travelling ionospheric disturbances, which are caused by atmosperic waves, mainly gravity waves.

Table 2.1 illustrates the dramatic changes in F-region characteristics on a diurnal basis, and throughout an 11 year solar cycle, with the latter variability taken from daytime measurements (Anderson & Fuller-Rowell, 1999).

Table 2.1: Ionospheric variability (Anderson and Fuller-Rowell)

Ionospheric Parameter	Diurnal (Mid-Latitude)	Solar Cycle (Daytime)
Maximum density	1×10^5 to 1×10^6 electrons cm^{-3} (factor of 10)	4×10^5 to 2×10^6 electrons cm^{-3} (factor of 5)
Maximum usable frequency	12 to 36 MHz (factor of 3)	21 to 42 MHz (factor of 2)
Total electron content	5 to 50×10^{16} electrons m^{-2} (factor of 10)	10 to 50×10^{16} electrons m^{-2} (factor of 5)

While the ionosphere can affect the signals from satellites which pass through it, the thermosphere can affect the motion of the satellites themselves. Increased solar activity, sometimes manifested in solar flares, can emit large quantities of electromagnetic radiation (mainly X-rays) and high energy particles (mainly protons). Along with ultraviolet radiation, X-rays heat up the thermosphere, causing it to expand, thus increasing the atmospheric pressure experienced by satellites and causing drag on their orbits. Geomagnetic storms[8] can cause even larger density changes - around 200 - 300%, compared to the 30% from solar flares. Low earth orbit, between 160 and 2,000 km, is in operation by the majority of satellites and all manned space stations, and such instruments may sometimes have to have their orbits boosted to account for this increased drag. To assess the atmosphere's influence on the satellite's orbit, many interdependent "drag coefficients" must be calculated, including the shape of the satellite, and atmospheric characteristics, such as the distribution of pressure and temperature (Vallado & Finkleman, 2014). Solar activity can have more direct impacts on technology, for instance charged particles emitted from the Sun can increase radiation levels and damage sensitive electronics. Solar flares have also been known to directly interfere with high frequency communication signals used by military and transport organisations.

Radio and satellite navigation users require detailed representations of the thermosphere in order to use their technologies with precision and confidence; the Met Office can provide them with these by modelling the whole atmosphere, coupled with the

[8] Geomagnetic storms: disturbance in the Earth's magnetosphere caused by a sudden change in the solar wind dynamic pressure at the magnetopause, which occurs when it is impacted by a coronal mass ejection or solar flare material.

ionosphere. While ENDGame currently does not model the ionosphere, it is to be coupled with ionospheric models once its ceiling has been extended and its modelling at these altitudes stabilised. This will allow for intricate dynamics of the thermosphere to be modelled and forecast, including the aforementioned influence from the atmosphere below it. The next chapter will discuss the Met Office's model and how it is especially distinct in relation to similar whole atmosphere models.

Chapter 3

Unified Model

3.1 ENDGame

3.1.1 Overview

While the UM is the Met Office's atmospheric model, concerned with broad elements such as dynamics, physics or chemistry, ENDGame is the UM's dynamical core. Based on its predecessor's semi-implicit semi-Lagrangian discretisations of the hydrostatic fully compressible Euler equations, ENDGame was designed as a more versatile suite of test environments. ENDGame allows for the UM to be switched between various setups, such as: hydrostatic and non-hydrostatic[1]; deep- and shallow-atmosphere; or spheroidal, spherical or Cartesian coordinate systems. It also uses semi-Lagrangian[2] advection and semi-implicit[3] time stepping (SISL). ENDGame's non-hydrostatic setting is a unique advantage it possesses among whole atmosphere models; non-hydrostatic dynamics are able to model thunderstorms, associated acoustic waves, and high frequency gravity waves (Deng & Ridley, 2011), phenomena which may be overlooked by hydrostatic models.

ENDGame features less damping than its predecessor and is therefore more accurate, particularly in its realisation of individual synoptic phenomena such as cyclones, fronts, troughs and jet streams. Improved scalability allows for increased resolution in line with increase of supercomputer power. The sub-grid size physical parameterisations have been revised to run with ENDGame,

[1] Hydrostatic models assume that the vertical pressure gradient is set equal to gravity times density.

[2] The Lagrangian numerical method describes the atmosphere in terms of individual air parcels, while a Eulerian method considers rates of change at spacial coordinates. A semi-Lagrangian system uses discretised equations developed from the Lagrangian method, but employed within a Eulerian spacial grid.

[3] Semi-implicit time stepping: technique which discretises a time-dependent system of equations with an implicit scheme for some terms and an explicit one for others. If done carefully this method can reduce computing time with no sacrifice to accuracy.

and ENDGame features higher resolution of data assimilation which defines the "initial state" of the atmosphere prior to running. Improvements were also made in the role of satellite data in this assimilation process.

ENDGame's numerical approach is largely the same as its predecessor, and it solves the same set of equations. However, a significant difference is its iterative approach; it uses an (already accurate) solution as a first guess, then computes successively better solutions by using its previous estimate as the first guess of the new estimate. It does this through the use of two iterative loops, which it applies twice per timestep.

In early 2015, ENDGame will commence operations in the Met Office's 1.5 km resolution UK regional forecasting system, as well as its short range and seasonal forecast. It will also be used for the atmospheric component of the Met Office's Earth system climate prediction model (Met Office, 2014). However, the test environment this project used for experiments has 60 km resolution. This has repercussions in its representation of gravity waves - because gravity waves start with wavelengths less than 60 km, they fall into the category of sub-grid phenomena and so are physically parametrised. ENDGame runs with an orographic[4] gravity wave scheme and can turn on a non-orographic scheme (the latter's effects are explored in Section 5.2.3). While the orographic scheme only represents waves from the surface up to 40 km altitude, the latter computes acceleration of mean flow from non-stationary entities, such as updrafts, and, rather than representing individual gravity waves, simulates the momentum deposition caused by a whole spectrum of waves as they propagate up through the atmosphere (Warner & McIntyre, 2001).

3.1.2 Governing equations

As with any attempt to capture a physical phenomenon mathematically, one must start with physical laws. From these, ENDGame's continuous equations are derived, which are discretised via finite difference and other methods, to be then computed by the Met Office's supercomputers. This section is based on the mathematics detailed in Wood et al.'s 2013 paper.

The continuous equations for a perfect gas, in vector form, are the following, where: u is the veclocity vector; θ is the potential temperature; ρ is density; V is an elemental fluid volume; $\pi \equiv (p/p_0)^{\kappa}$ is the Exner pressure where p is pressure and p_0 is a constant reference pressure; g is the apparent gravitational vector, which is the sum of actual gravity and the centrifugal force per unit mass; Ω is Earth's rotation vector; R is the gas constant per unit mass; c_p is the specific heat at constant pressure, and $\kappa \equiv R/c_p$. Also, the derivative $\frac{D}{Dt} \equiv \frac{\partial}{\partial t} + u \cdot \nabla$ is the material derivative.

[4] Orographic: relating to relief of mountains, hills and other significant terrain.

$$\frac{Du}{Dt} + 2\Omega \times u = -c_p \theta \nabla \pi + g \tag{3.1}$$

$$\frac{D\theta}{Dt} = 0 \tag{3.2}$$

$$\frac{D}{Dt}\left(\int_V \rho dV\right) = 0 \tag{3.3}$$

$$\pi^{(1-\kappa)/\kappa} = \left(\frac{R}{p_0}\right)\rho\theta \tag{3.4}$$

These are taken together with the kinematic equation, where x denotes spacial position,

$$\frac{Dx}{Dt} = u \tag{3.5}$$

which is required in advance of the discretisation.

Equations (3.1) – (3.4) are, respectively, the momentum, thermodynamic, continuity and state equations. Equation (3.3) is the integral equivalent of

$$\frac{D\rho}{Dt} + \rho \nabla \cdot u = 0$$

which is the more usual form of the continuity equation used in traditional SISL discretisations. Equations (3.1) - (3.5) are then discretised along a trajectory over a time period of $\triangle t$, approximating any residual integrals via a trapezoidal rule. This trapezoidal rule is subject to an off-centring parameter α, which will be explored further in Section 4.2.

Now is applied the discretisation to (3.1) - (3.3). Here, the superscripts n and n + 1 denote the time step, and subscripts A and D denote evaluation at the arrival and departure points respectively. This yields, for the discretisation of (3.1),

$$(u - \alpha \triangle t \psi)_A^{n+1} = (u + \beta \triangle t \psi)_D^n \tag{3.6}$$

where

$$\psi \equiv -2\Omega \times u - c_p \theta \nabla \pi + g$$

and

$$\beta = (1 - \alpha)$$

For the discretisation of (3.2) we have

$$\theta_A^{n+1} = \theta_D^n \tag{3.7}$$

and for the discretisation of (3.3) we have

$$\left(\int_V \rho dV\right)_A^{n+1} = \left(\int_V \rho dV\right)_D^n \tag{3.8}$$

Now, since ENDGame avoids a shallow atmosphere approximation, a rotation matrix M is now defined, the elements of which depend on the particular coordinate system. Equation (3.6) now becomes

$$(u - \alpha_u \triangle t \psi)_A^{n+1} = M\,(u + \beta_u \triangle t \psi)_{D_L}^n \tag{3.9}$$

Here, the subscript D_L denotes the evaluation at the departure point, but this time in terms of the local basis vectors at that departure point. There are also subscripts on the α and β off centring parameters, which indicate with which quantity they are associated.

Defining

$$\Psi = (\psi_u, \psi_v, \psi_w)$$

the components of the momentum equation (3.9) become

$$(u - \alpha_u \triangle t \Psi_u)_A^{n+1} = M_{11}\,(u + \beta_u \triangle t \Psi_u)_{D_L}^n + M_{12}\,(v + \beta_v \triangle t \Psi_v)_{D_L}^n + M_{13}\,(\delta_V w + \beta_w \triangle t \Psi_w)_{D_L}^n \tag{3.10}$$

$$(u - \alpha_v \triangle t \Psi_v)_A^{n+1} = M_{21}\,(u + \beta_u \triangle t \Psi_u)_{D_L}^n + M_{22}\,(v + \beta_v \triangle t \Psi_v)_{D_L}^n + M_{23}\,(\delta_V w + \beta_w \triangle t \Psi_w)_{D_L}^n \tag{3.11}$$

$$\left[(\partial_V + \mu \triangle t)\, w\right]_A^{n+1} - \left(\alpha_w \triangle t \Psi_w{}_A^{n+1}\right) = M_{31}\,(u + \beta_u \triangle t \Psi_u)_{D_L}^n + M_{12}\,(v + \beta_v \triangle t \Psi_v)_{D_L}^n + M_{13}\,(\delta_V w + \beta_w \triangle t \Psi_w)_{D_L}^n \tag{3.12}$$

Here, a non-hydrostatic switch, ∂_V has been introduced, which makes the equation set fully non-hydrostatic when $\partial_V = 1$

and quasi-hydrostatic when $\partial_V = 0$. A Rayleigh damping term, $-\mu w$, has been added to the right hand side of the w equation, which is discretised fully implicitly in time, eventually leading to the μw_A^{n+1} term on the left hand side of (3.12).

This is within a geopotential curvilinear orthogonal coordinate system, where the coordinates are denoted by ξ_1, ξ_2 and ξ_3 (with ξ_3 aligned with -g). The corresponding metric factors for this system are h_1, h_2 and h_3 respectively, and the components of the wind associated with each coordinate are denoted by

$$u_i \equiv h_i \frac{D\xi_i}{Dt} \tag{3.13}$$

for $i = 1, 2, 3$, where $(u_1, u_2, u_3) = (u, v, w)$. In this coordinate system,

$$\Psi_u = -2\left(\Omega \times u\right)_u - \frac{c_p\theta}{h_1}\left(\frac{\partial \xi_3}{\partial \eta}\right)^{-1} \times \left\{\frac{\partial}{\partial \xi_1}\left[\left(\frac{\partial \xi_3}{\partial \eta}\right)\pi\right] - \frac{\partial}{\partial \eta}\left[\left(\frac{\partial \xi_3}{\partial \xi_1}\right)\pi\right]\right\} \tag{3.14}$$

$$\Psi_v = -2\left(\Omega \times u\right)_v - \frac{c_p\theta}{h_2}\left(\frac{\partial \xi_3}{\partial \eta}\right)^{-1} \times \left\{\frac{\partial}{\partial \xi_2}\left[\left(\frac{\partial \xi_3}{\partial \eta}\right)\pi\right] - \frac{\partial}{\partial \eta}\left[\left(\frac{\partial \xi_3}{\partial \xi_2}\right)\pi\right]\right\} \tag{3.15}$$

$$\Psi_w = -2\left(\Omega \times u\right)_u - \frac{c_p\theta}{h_1}\left(\frac{\partial \xi_3}{\partial \eta}\right)^{-1} \frac{\partial \pi}{\partial \eta} - g \tag{3.16}$$

The kinematic equation (3.5) can be discretised in the same way as the momentum equation, so that it can be simply switchable between different coordinate systems. Let $\mathbf{r}$ be a position vector with $r = |\mathbf{r}|$ the radial distance. So $\mathbf{k} = \mathbf{r}/r$ defines the horizontal position of a point. Therefore (3.5) can be decomposed as

$$\frac{Dr}{Dt} = w \tag{3.17}$$

and

$$\frac{D\mathbf{k}}{Dt} = \frac{\mathbf{v}}{r} \tag{3.18}$$

where $\mathbf{v} = \mathbf{u} - \mathbf{k}(\mathbf{k}\cdot\mathbf{u})$ is the horizontal component of the velocity vector. In the terrain-following coordinate system, (3.17) is instead

$$\frac{D\eta}{Dt} = \dot{\eta} \tag{3.19}$$

The equations are then spacially discretized on an Arakawa C grid (see Figure 3.2) in the horizontal and a Charney – Phillips

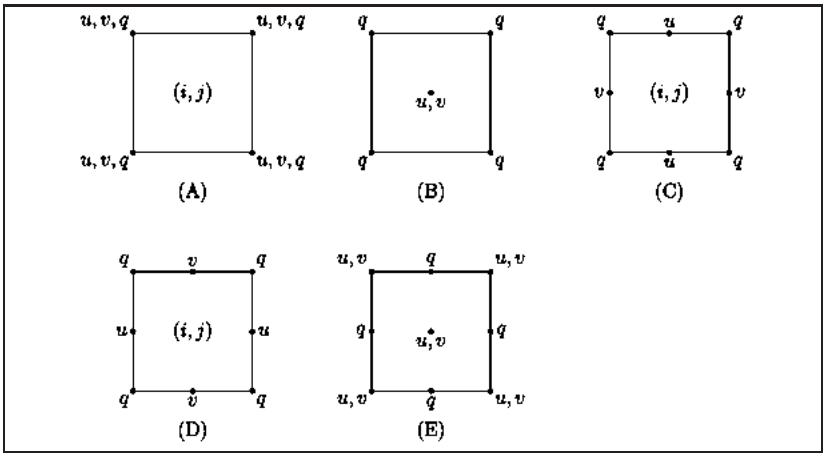

Figure 3.1: Depiction of Arakawa grid systems, illustrated on a generic grid cell. The "unstaggered" Arakawa A-grid evaluates all quantities at the same point on each grid cell, e.g., at the grid centre or at the grid corners; the "staggered" B-grid separates the evaluation of the two sets of quantities. e.g., velocities evaluated at the grid centre and masses at grid corners; the staggered C-grid further separates evaluation of vector quantities compared to the B-grid. e.g., instead of evaluating both east-west (u) and north-south (v) velocity components at the grid centre, one might evaluate the u components at the centres of the left and right grid faces, and the v components at the centers of the upper and lower grid faces; the D-grid is the C-grid but rotated 90°; D-grid is rotated 45°.

grid[5] in the vertical.

Of course, boundary conditions are needed, at the top and bottom levels. The fundamental condition is that, at the top and bottom levels, $\dot{\eta} = 0$. Also, it is assumed that there is zero vertical shear in the horizontal winds. Horizontal wind speed is assumed to be constant in the bottom and top half-layers, and a surface pressure, and by extension pressure gradient, are estimated. In the solution stage, the equations are averaged and solved over a grid, the size of which representing the resolution of the model. Processes which cannot be resolved by the grid boxes, such as convective clouds or rainfall, are dealt with by the model's physical parameterisations.

3.1.3 Model comparison

It is useful to establish the context into which ENDGame fits, in relation to its contemporary, equivalent models. There are a number of models which represent only the thermosphere and ionosphere, such as NASA's Global Ionosphere and Thermosphere Model (GITM), and the National Center for Atmospheric Research's Thermosphere Ionosphere Electrodynamics General Circulation Model (TIEGCM). However, these models do not represent the ionosphere's influence from phenomena below the thermosphere, as detailed in section 1.2. Models that do take such phenomena into account are "whole atmosphere" models, examples of which will be explored here.

[5] Charney–Phillips grid: a vertical grid setup which is considered good for capturing the potential vorticity dynamics and wave propagation

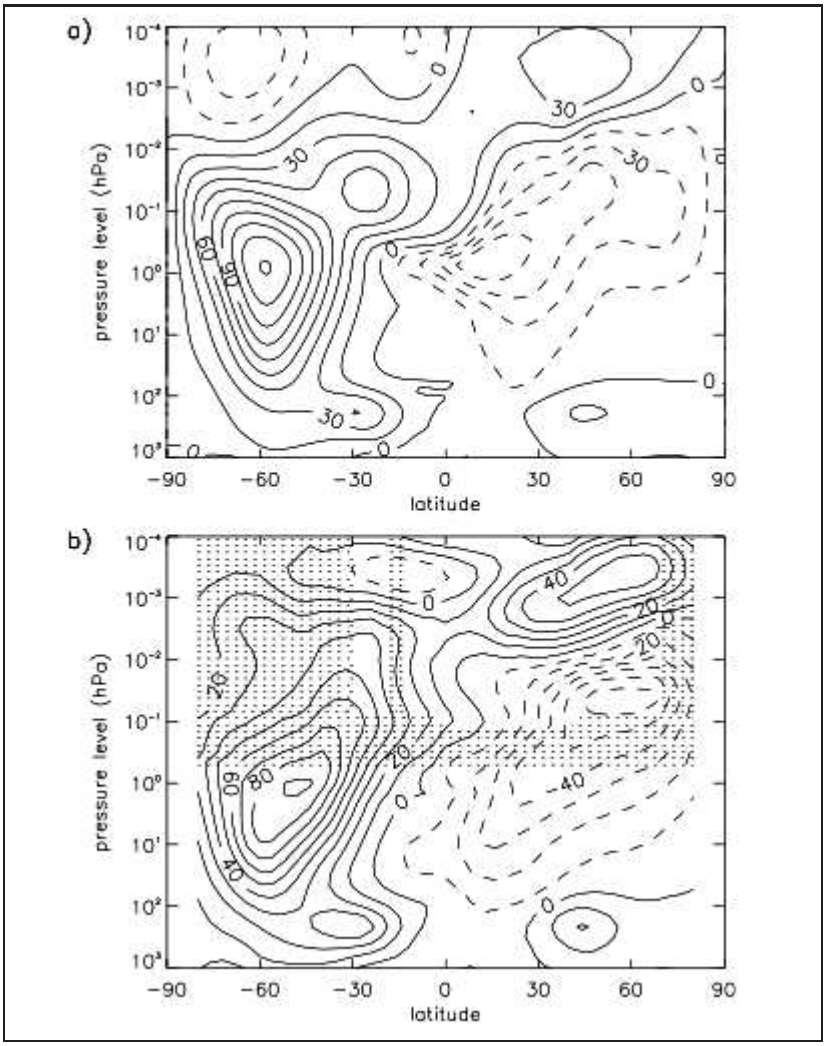

Figure 3.2: (a) WACCM zonal-mean zonal winds in ms^{-1} for July, averaged over 1990–99. (b) URAP climatological July zonal-mean winds. Shading in URAP winds indicates regions of insufficient observational coverage (Marsh et al., 2013). Similar comparisons will be made for ENDGame later in this paper.

Roble in his pioneering 2000 paper outlined the main areas from which a whole atmosphere model would both demand research and present benefits in realism and, therefore, accuracy:

"(1) physical,dynamical, and chemical interactions between the lower atmosphere and the upper atmosphere and ionosphere including transport of chemically and radiatively active species; (2) climate change in the upper atmosphere as well as the potential for upper layers to affect climate down below through "downward control"; (3) climate response to solar variability possibly through changes in middle and upper atmosphere chemistry and dynamics; (4) space weather or variability in thermosphere and ionosphere properties on shorter timescales driven by the lower atmospheric forcing and modulated by the solar and geomagnetic inputs from above; and (5) support and interpretation of satellite and ground-based observations spanning the entire domain."

(Roble, 2000).

A prominent numerical model which spans altitudes from the surface to the high atmosphere is the Whole Atmosphere Community Climate Model (WACCM). A central motivation to its development was to model the interations between atmospheric regions, for example wave phenomena which transport minor chemical species from the troposphere to higher layers. Further to this focus on dynamical interactivity and chemistry is, specifically, an investigation into the stratosphere and how it affects the depletion of the ozone layer. The model has achieved good agreement with observations in this regard (Marsh et al., 2013). Another process which the WACCM can model is solar variability and its effects on the upper and middle atmospheric regions, with the model in fact an upgrade on the aforementioned TIEGCM. The second whole atmosphere model which bears comparison is the Ground-to-topside model of Atmosphere and Ionosphere for Aeronomy (GAIA), which is the result of collaboration between several organisations in Japan, including the National Institute of Information and Communications Technology and Kyoto University. It is the result of the coupling of a whole atmosphere general circulation model (GCM), an ionospheric model, and an electrodynamics model. Its GCM covers the neutral atmosphere from the surface to the top of the thermosphere and tracks a set of physical processes which includes schemes for hydrology, a boundary layer, a radiative process, eddy diffusion, and moist convection. The timestep for the GCM is one minute, while for the ionospheric model it is half a second. The third model to be considered is the Whole Atmosphere Model, a GCM built upon an existing operational model used by the US National Weather Service. The model was developed to study and predict the effects of lower atmosphere dynamical processes on the ionosphere and upper atmosphere (Akmaev et al., 2010).

In terms of resolution, the ENDGame setting used in this project features 88 pressure levels for its 100 km ceiling setting, and 91 for 120 km, however, its current operation features 85 levels with an 85 km ceiling. In contrast, the atmospheric component of GAIA features 75 levels between the surface and the top of the thermosphere. WAM is the most resolved, with, roughly speaking, 100 layers below 100 km, and 50 layers in the thermosphere, where the vertical extent and resolution of the grid are an input parameter which can be changed. WACCM-X has 81 pressure levels (Akmaev, 2011).

Efforts are underway to improve ENDGame's chemistry schemes, simply because the chemical composition of the mesosphere and thermosphere are not represented by the existing schemes. The UM's current chemistry scheme models the mixing of a variety of aerosol species, in a coupled tropospheric-stratospheric chemistry-climate model; the mesosphere and thermosphere are not yet modelled chemically. Separate equations are needed for above the turbopause[6]. Chemical changes are important: for example, the ratio between O and N_2 influences the plasma density of the ionosphere's F region (Jackson, 2012). Other models may have an advantage over ENDGame in regards to chemistry. WACCM was designed with chemistry modelling, particularly of ozone layer depletion, as a key objective. WACCM-X (the most recent version) integrates a three-dimensional photochemical transport model, with ion species. In GAIA, thermospheric major neutral species O, O_2, and N_2 are prescribed, as well as

[6] Turbopause: a boundary, close to the mesopause at roughly 100 km altitude, below which turbulent mixing dominates, and above which is dominated by molecular diffusion and chemical composition varies corresponding to different chemical species.

radiatively active gases O_3,CO_2 and NO. WAM treats major species O, O_2, and N_2 self-consistently, including large-scale transport, oxygen chemistry, and mutual diffusion both in vertical and horizontal directions. Ozone is transported in WAM, and a linearized Ozone Photochemistry Parameterization is employed on the basis of a two-dimensional middle atmospheric photochemical model. Other radiatively active species are also prescribed empirically (Akmaev, 2011).

Also, in ENDGame, the assumption of local thermodynamic equilibrium (LTE)[7] is made in terms of the radiation scheme, and, like all physical assumptions, sacrifices realism for simplicity to some degree. The introduction of a non-LTE radiation scheme is an objective of ENDGame's further development, with the aim to capture actions which occur in non-LTE situations; for example, calculating the solar heating of carbon dioxide in the near-infrared bands demands consideration of non-LTE effects (Fomichev, 2004). WACCM has implemented longwave LTE radiation schemes for the first 40 km of its modelled atmosphere, while WAM can account for non-LTE infrared heating.

However, the fundamental advantage that ENDGame possesses over its counterparts is its non-hydrostatic setup. All three models, GAIA (Jin et al., 2011), WAM (Akmaev et al., 2010) and WACCM (Burns et al., 2011), operate with the hydrostatic approximation. This approximation, as mentioned, eliminates vertically propagating acoustic waves, and distorts and overestimates gravity waves. The approximation is set to become more problematic as models develop, since as the horizontal resolution of a model increases, the hydrostatic approximation becomes less justified (Akmaev, 2011). While ENDGame's non-hydrostatic setup will give it a clear advantage, it is currently not without stability drawbacks with thermospheric upper boundaries; in Chapter 4, I present the results from my stability experiments with ENDGame.

[7] Local thermodynamic equilibrium: the assumption that all ionisations, excitations and velocities are in equilibrium, corresponding to the local temperature.

Chapter 4

Stability experiments

The method I employed when attempting improvements of stability was the following: I would change the initial run setup via the UMUI (see Figure 4.1), altering a given parameter; I would then submit the run to the supercomputer's job queue; this job would then simulate the atmosphere from an initial state, taken from a 21 September 1981 dataset; the simulation would run until it crashed, at which point output files would be produced, giving the total number of timesteps successfully computed before the job crashed.

4.1 100 km ceiling

At the beginning of my experiments, I loaded the 88 vertical pressure level domain into the initial setup, thus extending the ceiling to 100 km. I then altered the timestep, and the resubmission pattern - both of which had an impact on stability. The timestep is the amount of time in the simulation which elapses before a new state of the atmosphere is computed. The resubmission pattern is the limit on the amount of real time the supercompu ter will remain on one job - if this time is exceeded, the job will be resubmitt ed to the back of the queue, and the supercomputer will pick up where it left off when the job returns to the front of the queue. Unfortunately I experienced a lot of early crashes and lack of output in the initial runs, so did not gather substantial results. Table 4.1 summarises my stability results with a 100 km ceiling.

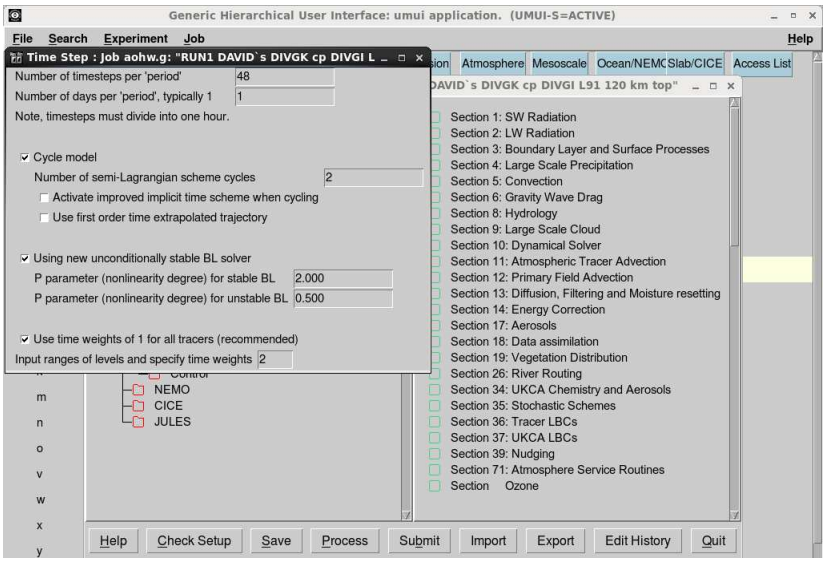

Figure 4.1: Screenshot of the UM's user interface (UMUI), with the foreground window allowing changes to the run's timestep, and background window showing physical parameter sections, which can be changed. Processing and then submitting a run will send it to a queue, to be computed by the Met Office's Power7 IBM supercomputer.

Table 4.1: 100 km ceiling stability runs

Run number	Changes	Timestep crashed
1	10 min timestep	20 days
2	5 min timestep	Wallclock limit reached
3	5 min timestep, 14 day resubmission	75 days
4	5 min timestep, 12 day resubmission	Crashed very early
5	2.5 min timestep, 7 day resubmission	261 days

While my most stable run was 261 days, this wasn't the most stable run completed with 100 km - David Jackson had previously discovered a configuration which ran for over a year. This is the run upon which I would perform validity checks in the next chapter.

4.2 120 km ceiling

For my 120 km ceiling stability experiments, I loaded a 91 pressure level domain to raise the ceiling. I employed the same method as in the 100 km ceiling experiments, but due to the even lower pressure of the atmosphere of such heights, it was advised that I alter parameters which offset the impact this miniscule pressure would have on the speed of the winds.

The first of these parameters is α, an off-centring parameter. To illustrate, consider the general representation of equation (3.6)

$$\frac{DF}{Dt} = G,$$

where F and G could be either both scalar or both vector fields. Integrating this along a trajectory over a time interval $\triangle t$ gives

$${}_t\int^{t+\triangle t} \frac{DF}{Dt} dt = {}_t\int^{t+\triangle t} G dt,$$

which can be rewritten as

$$F(x^{t+\triangle t}, t+\triangle t) - F(x^t, t) = {}_t\int^{t+\triangle t} G dt$$

where $x^{t+\triangle t}$ is the position along any particular trajectory at time $t+\triangle t$. The right hand side is then approximated to give

$$F(x^{t+\triangle t}, t+\triangle t) - F(x^t, t) = \triangle t \left[\alpha G(x^{t+\triangle t}, t+\triangle t) + (1-\alpha) G(x^t, t)\right].$$

Here, α is an off-centring parameter. It determines the balance between an explicit solution and an implicit, taking the null value for a fully explicit and unity for a fully implicit.

The second parameter I altered was the vertical damping coefficient. The vertical damping of vertical velocities is

$$w^{t+\triangle t} = w^t - R_w \triangle t w^{t+\triangle t},$$

where w^t and $w^{t+\triangle t}$ is the vertical velocity at the current and next timestep. R_w is the vertical damping coefficient and in effect produces a "sponge layer" at the top of the atmosphere to damp vertical velocities. The spacial coverage and value of the vertical damping coefficient is determined by

$$R_w = \begin{cases} C \sin^2\left(0.5\pi(\eta - \eta_s)\left(\frac{1.0}{1.0-\eta_s}\right)\right), & \eta \geq \eta_s \\ 0, & \eta < \eta_s \end{cases},$$

where η is non-dimensional height, η_s is the start height for the sponge layer, and C is the maximum damping present at the upper boundary. Table 4.2 details the effect that α and the variable damping coefficient has on stability.

Table 4.2: 120 km ceiling stability runs

Run number	Changes	Timestep crashed
1	2.5 min, 7 day resubmission	11 days
2	30 min timestep, 1 month resubmission, alpha=0.55 (default 0.7)	1
3	30 min timestep, 1 month resubmission, alpha=0.6	2
4	30 min timestep, 1 month resubmission, alpha=0.82	2
5	30 min timestep, 1 month resubmission, alpha=0.88	2
6	30 min timestep, 1 month resubmission, alpha=0.9	393
7	20 min timestep, 1 month resubmission, alpha=0.9	317
8	20 min timestep, 1 month resubmission, alpha=0.85	3
9	60 min timestep, 1 month resubmission, alpha=0.9	1
10	30 min timestep, 1 month resubmission, alpha=0.93	452
11	30 min timestep, 1 month resubmission, alpha=0.94	470
12	30 min timestep, 1 month resubmission, alpha=0.95	464
13	30 min timestep, 1 month resubmission, alpha=0.96	597
14	30 min timestep, 1 month resubmission, alpha=0.935	473
15	30 min timestep, 1 month resubmission, alpha=0.945	344
16	30 min timestep, 1 month resubmission, alpha=0.97	592
17	30 min timestep, 1 month resubmission, alpha=0.98	653
18	30 min timestep, 1 month resubmission, alpha=0.99	720 (memory cap)
19	5 min timestep, 1 month resubmission, alpha=0.99	448
20	10 min timestep, 1 month resubmission, alpha=0.99	96
21	20 min timestep, 1 month resubmission, alpha=0.99	351
22	30 min timestep, 7 day resubmission, alpha=0.9	6
23	30 min timestep, 1 month resubmission, alpha=0.99, vertical damping from 0.05 to 0.1	501
24	30 min timestep, 1 month resubmission, alpha=0.99, vertical damping = 0.15	1005
25	30 min timestep, 1 month resubmission, alpha=0.99, vertical damping = 0.2	1029
26	30 min timestep, 1 month resubmission, alpha=0.99, vertical damping = 0.25	986
27	30 min timestep, 1 month resubmission, alpha=0.99, vertical damping = 0.3	623
28	30 min timestep, 1 month resubmission, alpha=0.99, vertical damping = 0.35	954

Run number	Changes	Timestep crashed
29	30 min timestep, 1 month resubmission, alpha=0.99, vertical damping = 0.4	1063 (22.1 days)
30	30 min timestep, 1 month resubmission, alpha=0.99, vertical damping = 0.5	1053
31	30 min timestep, 1 month resubmission, alpha=0.99, vertical damping = 0.6	967
32	30 min timestep, 1 month resubmission, alpha=0.99, vertical damping = 0.7	1036
33	30 min timestep, 1 month resubmission, alpha=0.99, vertical damping = 0.8	1183 (24.6 days)
34	30 min timestep, 1 month resubmission, alpha=0.99, vertical damping = 0.9	1110
35	30 min timestep, 1 month resubmission, alpha=0.99, vertical damping = 1.0	5
36	30 min timestep, 1 month resubmission, alpha=0.99, vertical damping = 0.78	1367
37	30 min timestep, 1 month resubmission, alpha=0.99, vertical damping = 0.82	1085
38	30 min timestep, 1 month resubmission, alpha=0.99, vertical damping = 0.77	1117
39	30 min timestep, 1 month resubmission, alpha=0.99, vertical damping = 0.79	1146
40	30 min timestep, 1 month resubmission, alpha=0.99, vertical damping = 0.78,solver tolerance 1e-6	No output
41	30 min timestep, 1 month resubmission, alpha=0.99, vertical damping = 0.78,solver tolerance 1e-7	No output
42	30 min timestep, 1 month resubmission, alpha=0.99, vertical damping = 0.78, solver tolerance 1e-5 (back to default), spin up from 15 October	296
43	30 min timestep, 1 week resubmission, alpha=0.99, vertical damping = 0.78	336
44	30 min timestep, 1 month resubmission, alpha=0.99, vertical damping = 0.78	474
45	30 min timestep, 1 month resubmission, alpha=0.99, vertical damping = 0.78	1367
46	30 min timestep, 1 month resubmission, alpha=0.99, vertical damping = 0.785	1414
47	30 min timestep, 1 month resubmission, alpha=0.99, vertical damping = 0.786	1262
48	30 min timestep, 1 month resubmission, alpha=0.99, vertical damping = 0.7855	1209
49	30 min timestep, 1 month resubmission, alpha=0.99, vertical damping = 0.7852	1082
50	30 min timestep, 1 month resubmission, alpha=0.99, vertical damping = 0.7845	1198
52	30 min timestep, 1 month resubmission, alpha=0.99, vertical damping = 0.7847	1162
52	30 min timestep, 1 month resubmission, alpha=0.99, vertical damping = 0.784	1043

While I was unable to visualise and determine the specific cause of the crashes for each run, the vast majority of the runs' output files cite "mass conservation error" and "floating point exception" as the reason for their crashes, which can be interpreted as unnaturally fast air speed. It was, therefore, well advised to attempt to damp the atmosphere. The two main conclusions to be drawn from the 120 km experiments are thus: firstly, increasing the alpha number, and therefore the numerical solver's

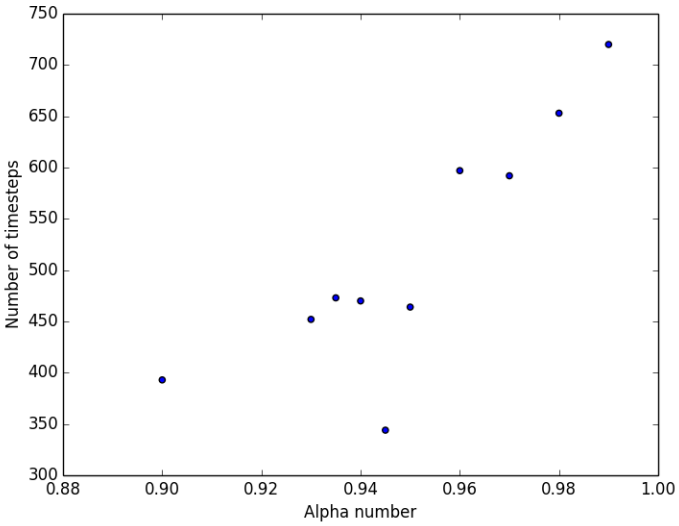

Figure 4.2: Summary scatter plot of stability experiments from first 23 runs, discounting anomolous runs, showing the number of timesteps computed before crashing against value of α. These data points only include runs with a 30 minute timestep and 1 month resubmission

implicitness, increases the run's stability (see Figure 4.2). Secondly, when applying increased damping to a setup with an almost completely implicit solver, there seems to be a "sweet spot" of 0.785, which gives significantly higher stability than higher or lower values, contradicting what one would intuitively expect would be a simple positive correlation. Conversely, there appears to be two values of the vertical damping coefficient which produce significantly lower instability. This is illustrated in Figure 4.3. This phenomenon may be similar to the "successive over-relaxation", seen in numerical linear algebra.

Timestep 1414 equates to 29.45 days of simulated atmosphere, which, at the time of writing, is the most stable run achieved with a 120 km ceiling. In my subsequent validation checks, this is the run I will take outputs from. Firstly, however, I will judge the validity of the most stable 100 km ceiling run achieved thus far, from David Jackson's own experiments.

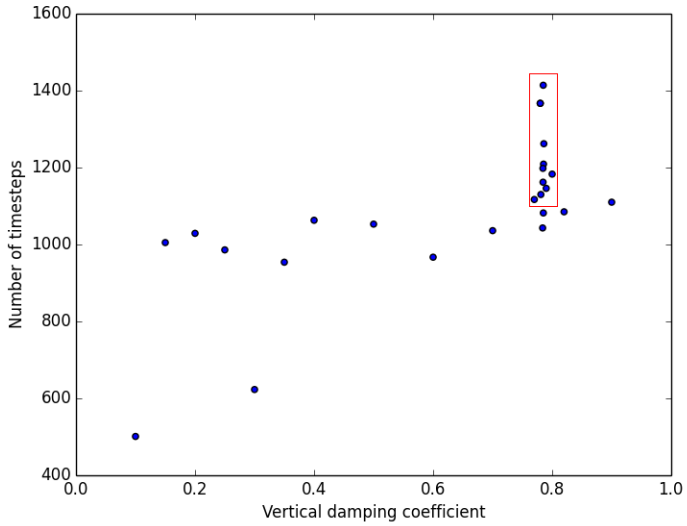

Figure 4.3: Summary scatter plot of stability experiments from run 23 onwards, discounting anomolous runs, showing number of timesteps computed before crashing against the vertical damping coefficient value. The area enclosed in the red box is enlarged in Figure 4.4.

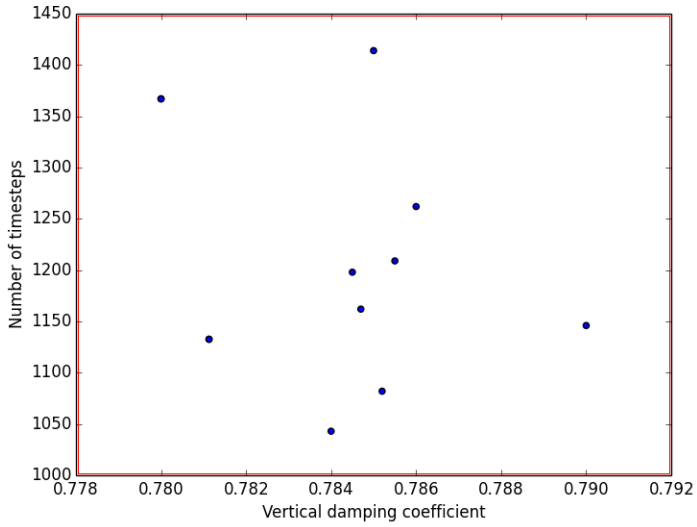

Figure 4.4: Enlarged plot of red boxed area from Figure 4.3.

4.2.1 Rayleigh damping of u and v winds

Another possible method for achieving improved stability, as recommended to me by Prof. John Thuburn, is to introduce Rayleigh damping to the horizontal u- and v-winds. As previously mentioned, the cause for the crashes is almost invariably given as "floating point exception" and "mass consevation error" - both of which are indicative of wind speeds which are too fast for the solver to work.

Introducing Rayleigh damping, of the same kind as already implemented for the vertical w-winds, involves copying a "branch" of the UM's code into a local directory for editing. Then the job is edited in the UMUI so it refers to this copied branch, instead of the usual location of the complete UM code. A damping profile matrix is allocated for both u and v, which acts as a rolling average of the wind profile. The winds in the upper two thirds of the atmosphere are then damped back to this profile:

u_damp(:,:,k) = (real(timestep_number-1)*u_damp(:,:,k) + u(:,:,k))/real(timestep_number)

v_damp(:,:,k) = (real(timestep_number-1)*v_damp(:,:,k) + v(:,:,k))/real(timestep_number)

As one could imagine, adding an element to such complex and interdependent code incurs follow-up additions and editing. The files edited were: eg_helm_rhs_star.f90, atm_step_4A.f90, init_vert_damp_mod.f90, as well as the hand edit file in my local directory, whose "EG_VERT_DAMP_PROFILE" line had to be changed.

The results of these changes were successful submission and compilation of code. However, only the first timestep is computed before the run crashes. The .leave output file mentions "floating point exception", as in previous runs, but offsets in many procedures also. In comparison, the longest run with a 120 km run only mentions one line with an offset in one procedure - this run has thousands of lines, revealing offset in many different files. I do not know what this error signifies, because the run compiles correctly and so I assume that the new code is implemented correctly. Unfortunately this was discovered too close to the end of my project to follow up on, however it is an open avenue of research which can be continued.

Chapter 5

Validation

5.1 100 km ceiling

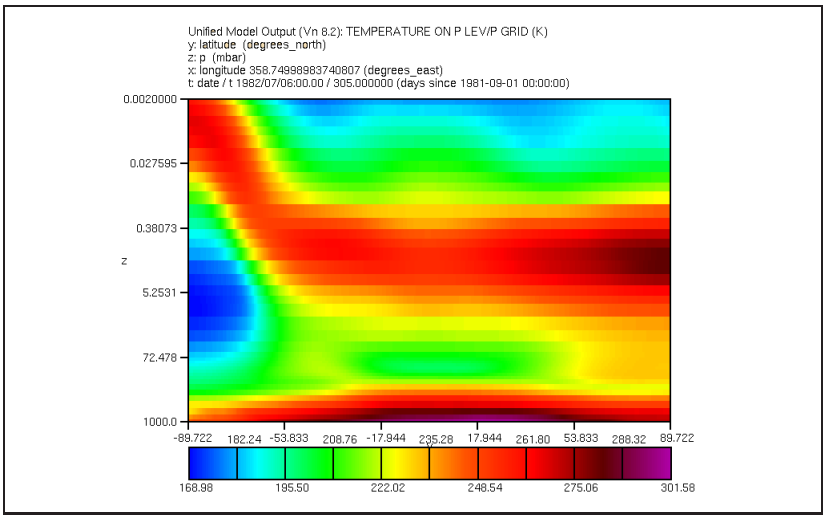

Figure 5.1: A typical output from the UM. There are many variables which can be tracked, and many ways to visualise and analyse them; here, the zonal mean temperature is outputted (the zonal mean is the average taken along a circle of latitude, i.e. in the west-east direction). The pole-to-pole latitude is along the x-axis and the log of the pressure level (to counter the exponential pressure decrease) is along the y-axis. As such, this plot doesn't represent a 2D slice of the temperature of the atmosphere as would be seen naturally, because the grid follows pressure, which, geographically, varies significantly.

5.2.1 Temperature

The model's temperature output (see Figure 5.1) was compared with the same data as observed by the Microwave Limb

Sounder (MLS) instrument aboard NASA's Aura satellite. MLS data was provided by Corwin Wright at the University of Bath. As stated by Waters et al.:

"The Earth Observing System Microwave Limb Sounder measures several atmospheric chemical species (OH, HO 2 ,H 2 O, O 3 , HCl, ClO, HOCl, BrO, HNO 3 ,N 2 O, CO, HCN, CH 3 CN, volcanic SO 2), cloud ice, temperature, and geopotential height to improve our understanding of stratospheric ozone chemistry, the interaction of composition and climate, and pollution in the upper troposphere. All measurements are made simultaneously and continuously, during both day and night. The instrument uses heterodyne radiometers that observe thermal emission from the atmospheric limb in broad spectral regions centered near 118, 190, 240, and 640 GHz, and 2.5 THz. It was launched July 15, 2004 on the National Aeronautics and Space Administration's Aura satellite and started full-up science operations on August 13, 2004. An atmospheric limb scan and radiometric calibration for all bands are performed routinely every 25 s. Vertical profiles are retrieved every 165 km along the suborbital track, covering 82 S to 82 N latitudes on each orbit. Instrument performance to date has been excellent." (Waters et al., 2006)

Subsequent validation of the MLS datasets have revealed good agreement, with temperature precision of 1 K or better from 316 hPa to 3.16 hPa, degrading to around 3 K at 0.001 hPa. (Schwartz et al., 2008)

Plotted below (see Figures 5.2, 5.3, 5.4 & 5.5) are contours of these data, with all model (left) and MLS data (middle) plotted on the same colour range, and all difference plots (right) on another colour range. The model data are taken from Prof. David Jackson's setup which ran for over a year. In this run, the non-orographic gravity scheme was turned off..

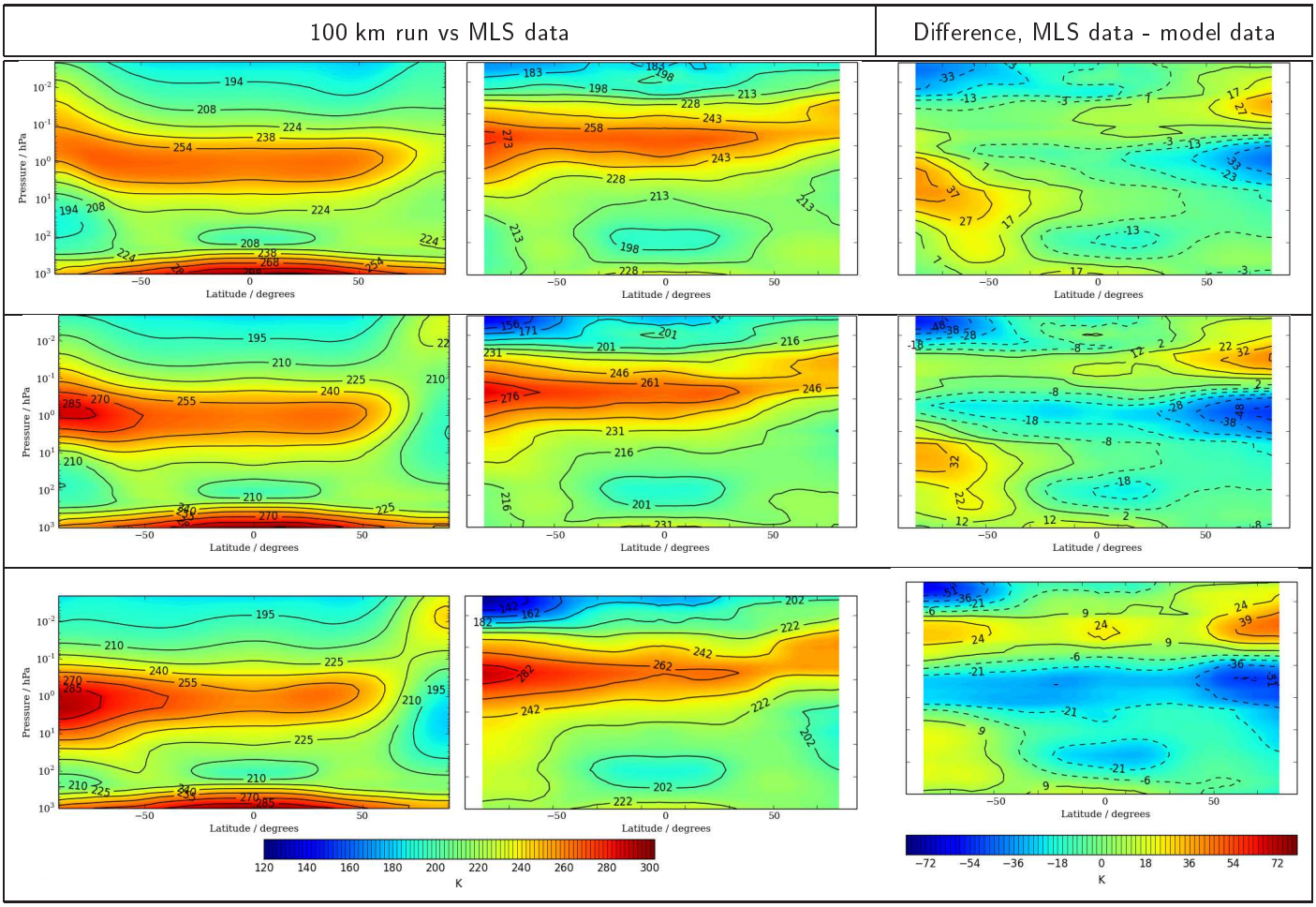

Figure 5.2: 100 km ceiling zonal mean temperature plots, October to December 1981, MLS observations, October to December 2004. First column model data, second column MLS data, third column difference, first row October, second row November, third row December.

The main impression to notice in Figure 5.2 is how well the model represents all major features of the temperature structure. The main differences are the absence of a volume of thermospheric cold air at the south pole, which is present in the MLS data, and the lower altitude of the large mesospheric warm air structure. A noteworthy phenomenon is the presence of warm tropospheric air, which is absent in the MLS data; this is an artifact of the instrument's downward extrapolation, so its presence in the model is in fact realistic.

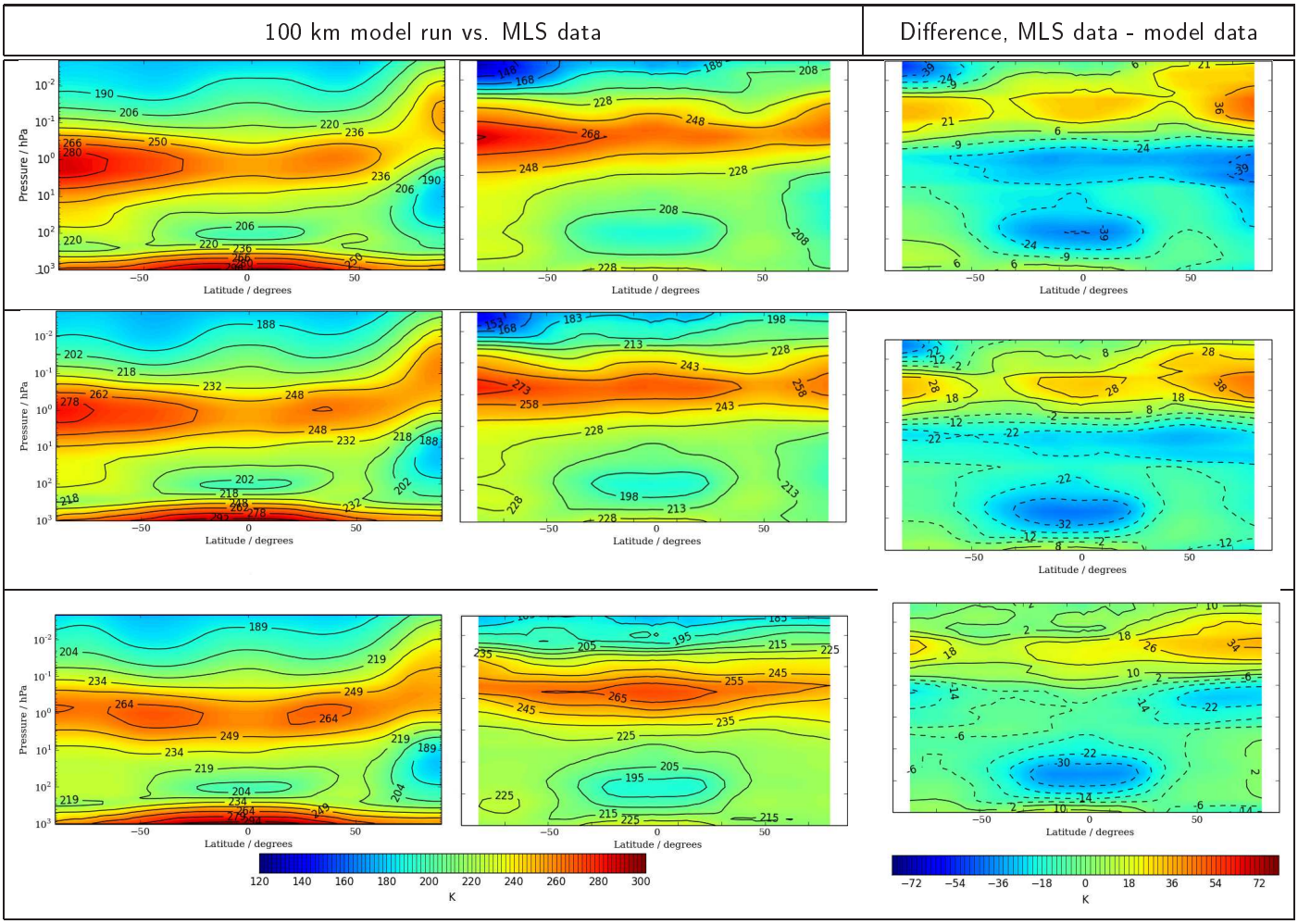

Figure 5.3: 100 km ceiling zonal mean temperature plots, January to March 1982, MLS observations January to March 2005. First column model data, second column MLS data, third column difference, first row January, second row February, third row March.

In Figure 5.3, featuring temperatures from January to March, again the thermospheric southern cold volume is not represented, until March where it is no longer observed. As before, the mesospheric warm air structure is lower than observed. There is also the presence of a cold north pole volume in February and March which is absent in observations.

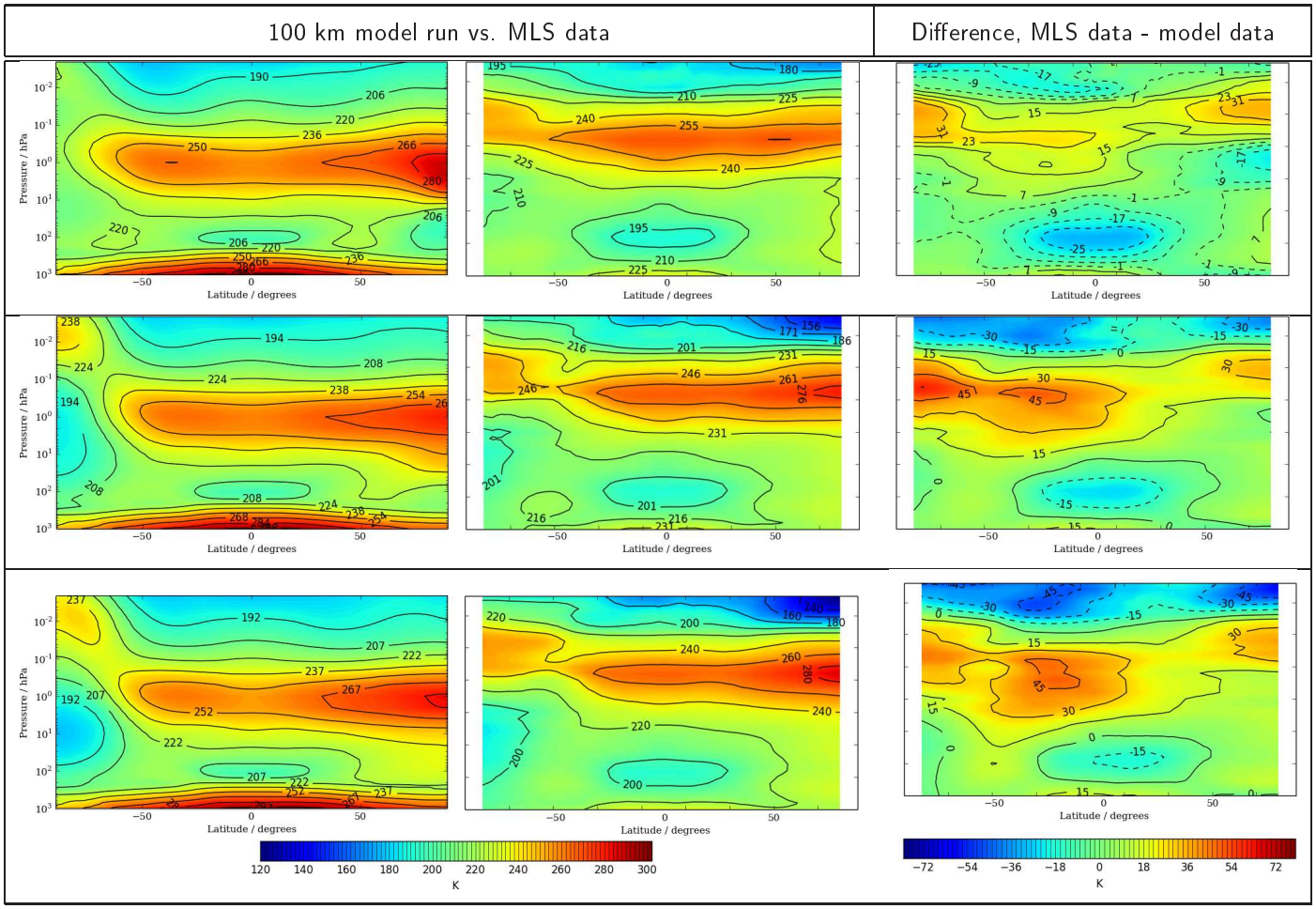

Figure 5.4: 100 km ceiling zonal mean temperature plots, April to June 1982, MLS observations April to June 2005. First column model data, second column MLS data, third column difference, first row April, second row May, third row June.

In Figure 5.4, featuring temperature comparisons from April to June, we see a return of the thermospheric cold volume which is absent in the model, however this time at the north pole. In June we see the beginning of a significant deviation in the model from observations - a volume of cold air at the south pole which is not as pronounced in the observations. All other structures are well represented, albeit with the major warm cross-latitudinal structure lower in the model than observed.

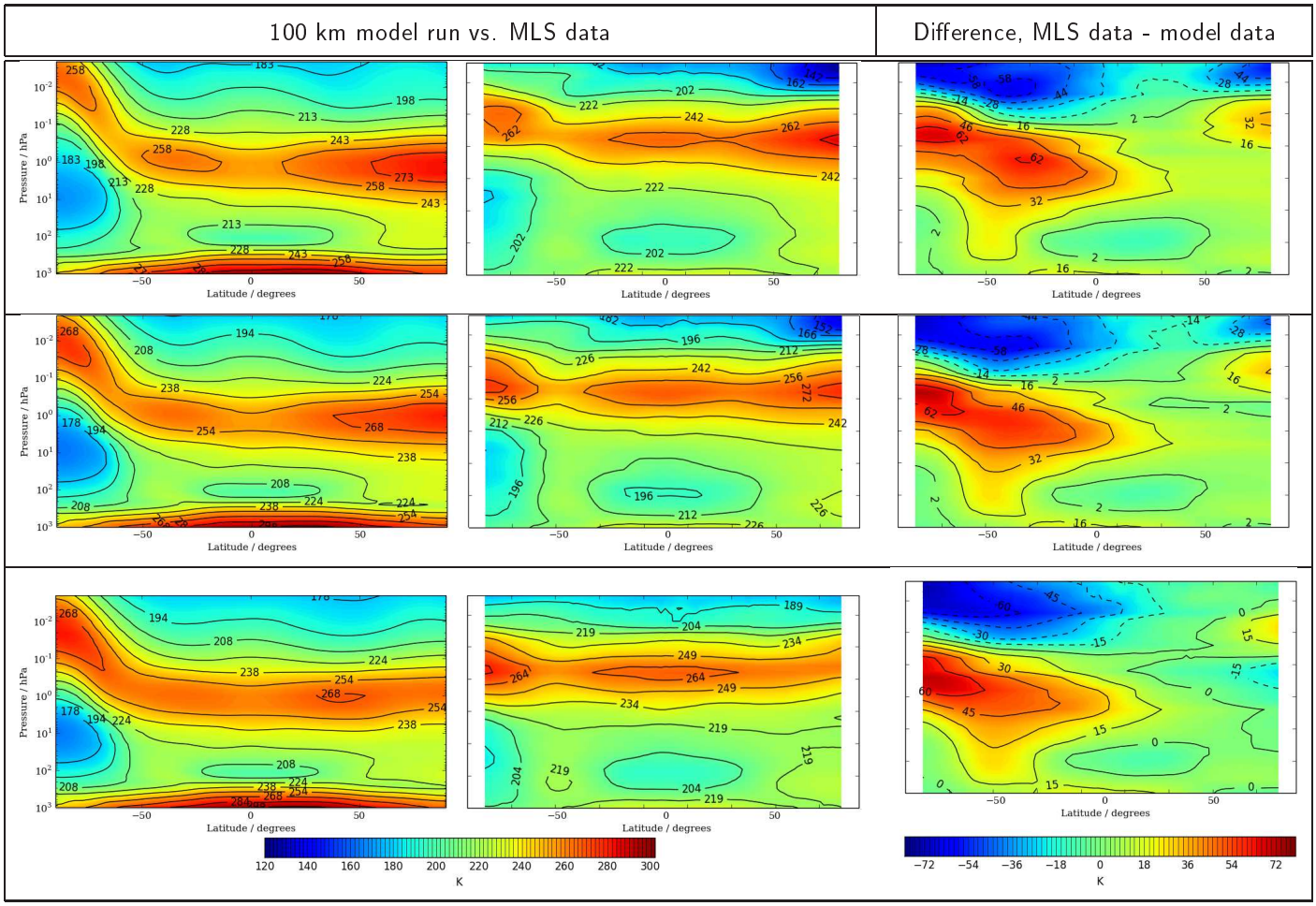

Figure 5.5: 100 km ceiling zonal mean temperature plots, July to September 1982, MLS observations July to September 2005. First column model data, second column MLS data, third column difference, first row July, second row August, third row September.

A prominent feature of the July to September temperatures (i.e. the winter temperatures in the southern hemisphere) is the volume of colder air in the model, relative to observations, at stratospheric altitude, at southern latitudes (see Figure 5.5). This could be a manifestation of the "cold pole problem", which is a recognised phenomena in other models, including WACCM. This occurs when the winter polar vortex is too strong and breaks down too late, resulting in colder south pole stratosphere temperatures than is observed. This could also be the reason for the cold north pole noted back in February and March (see Figure 5.3). Tan et al. speculate that this may be due to lack of westward wave forcing, and they suggest gravity waves which break in the stratosphere could help solve the problem by compensating for missing forcing (Tan et al., 2012). This effect will be investigated in Section 5.2.3.

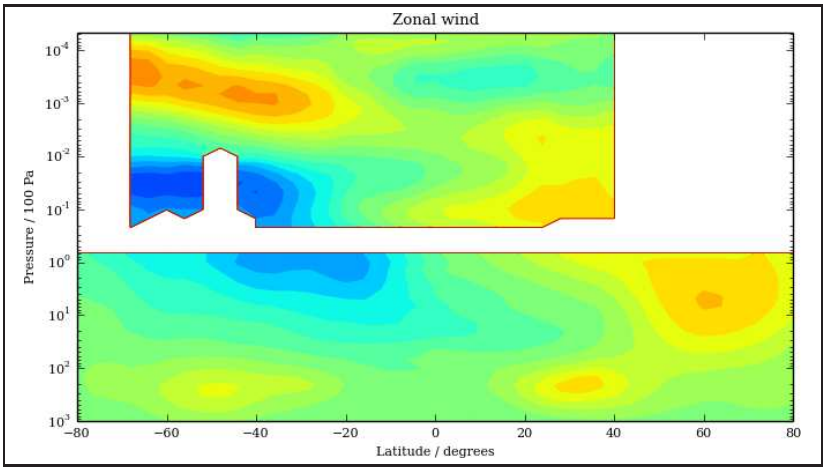

Figure 5.6: Example plot of zonal wind taken from the URAP data set. Shown here are the reliable areas of the plot, with the blank area representing areas with unreliable or insufficient data. These blank areas havbe been filled in via interpolation and climatological methods.

5.2.2 Zonal mean U-winds

Here, the 100 km run data is compared with data from UARS Reference Atmosphere Project (URAP). While the time interval for both datasets are from October to September, the URAP data is over 2004 to 2005. As such, this comparison should be treated with caution, because jet structures can change each year. The URAP data features parts of the data set which have been obtained through interpolation or climatology (see Figure 5.6). Also it should be noted that the URAP data covers a higher altitude of atmosphere. Again, plotted below (see Figures 5.7, 5.8, 5.9 & 5.10) are contours, with model and URAP data plotted on the same colour range, and all difference plots on another colour range.

http://uars.gsfc.nasa.gov/Analysis/UARS/urap/useful_publications/URAP_winds_ps.pdf

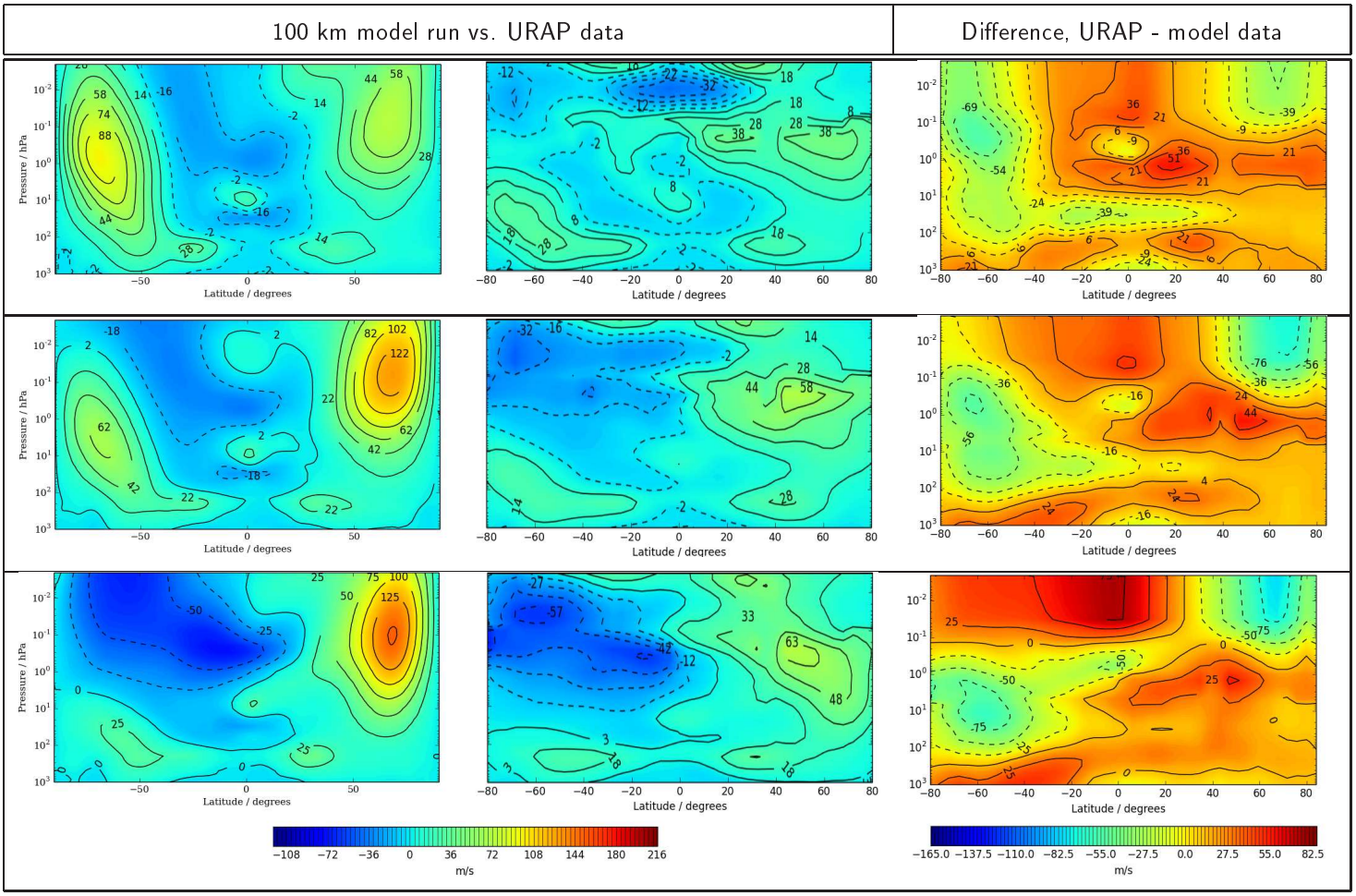

Figure 5.7: 100 km ceiling zonal mean U wind plots, October to December 1981, URAP observations October to December 1992. First column model data, second column URAP data, third column difference, first row October, second row November, third row December.

The obvious difference between the model data and the observations is the anomalous easterly jet in southern latitudes, whose volume and speed is significantly overestimated in the model (see Figure 5.7). This may be related to the aforementioned cold pole problem, since it occurs in the same location, at the same time of year. Tian noted in 2004 that this happened in the UM, and, due to a thermal wind relation, a southern polar jet was modelled to be 20 ms^{-1} faster than observed (Tian, 2004). Non-orographic gravity wave schemes have been known to alleviate anomalous estimation due to the cold pole problem (Tian, 2004), agreed with by Tan et al. as previously mentioned. The broad difference is that the model represents fewer, larger and faster jets, compared with the observed jets which are more numerous, smaller and slower.

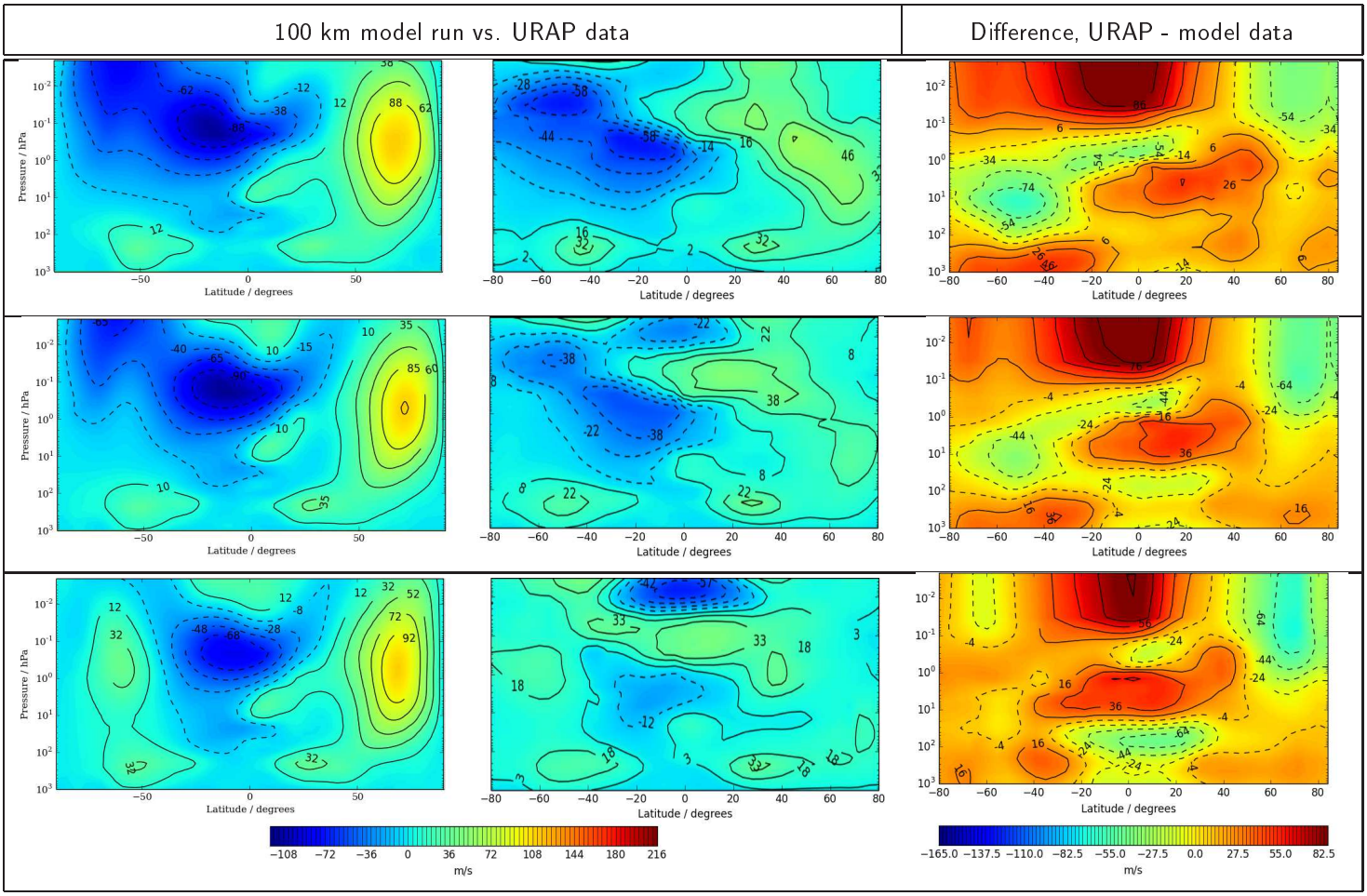

Figure 5.8: 100 km ceiling zonal mean U wind plots, January to March 1982, URAP observations January to March 1993. First column model data, second column URAP data, third column difference, first row January, second row February, third row March.

In January, the model offers a reasonable representation of some atmospheric wind structures (see figure 5.8). However, throughout the winter months of the northern hemisphere, this structure does not change as dramatically as it does in the observed data. In the observed winds, strong easterlies diminish in northern latitudes, and develop in equatorial latitudes, which does not happen in the model.

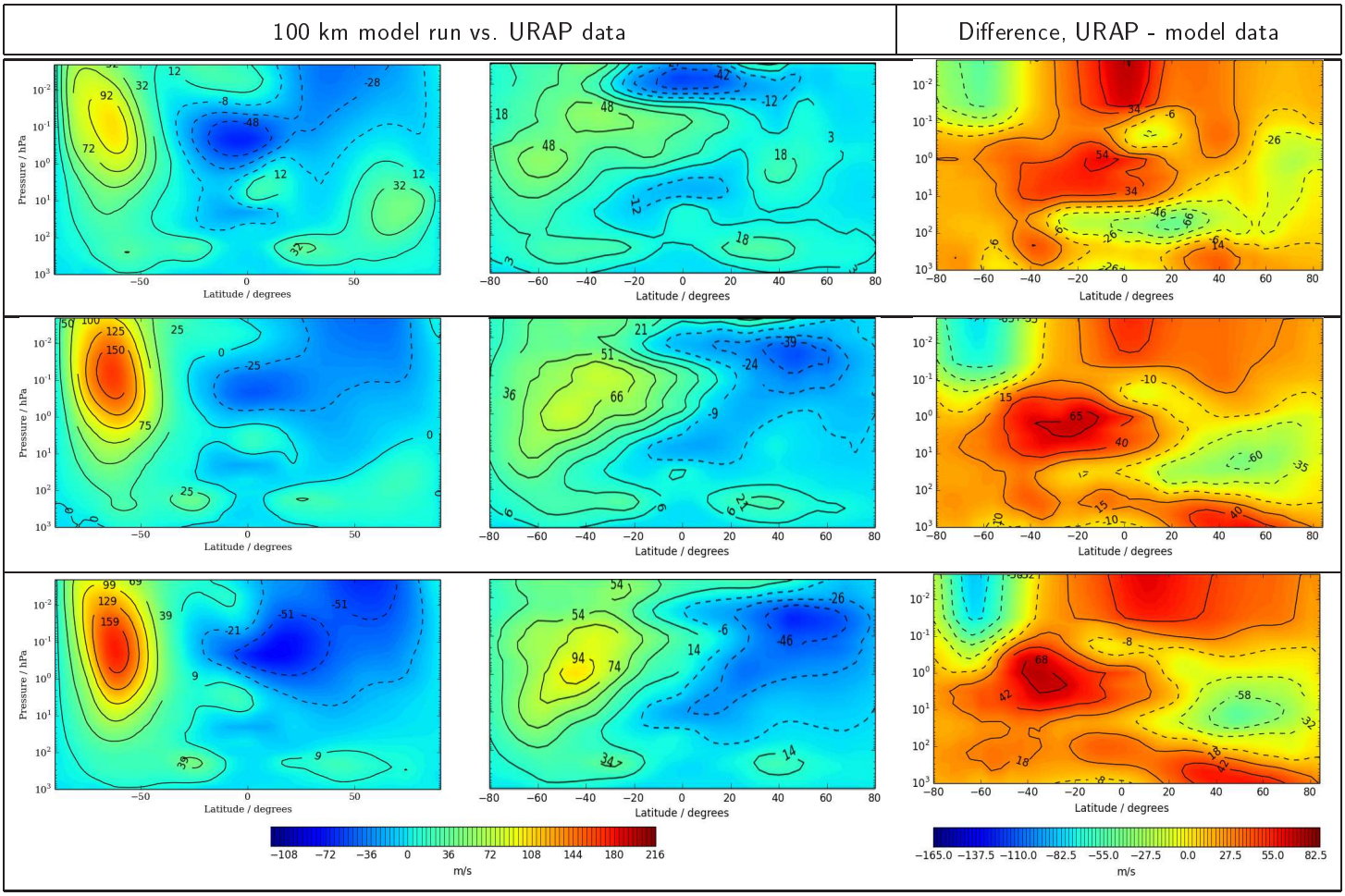

Figure 5.9: 100 km ceiling zonal mean U wind plots, April to June 1982, URAP observations April to June 1993. First column model data, second column URAP data, third column difference, first row April, second row May, third row June.

By May, the aforementioned easterly jet has merged with the major easterly in southern latitudes, and the model is broadly effective in representing wind structures (see Figure 5.9). However, the speed of this southern mesospheric jet is higher than the observed speed; again, possibly caused by gravity wave influence. Westerly jets are generally well represented in speed and structure, however in June the equatorial westerly is significantly faster than observed.

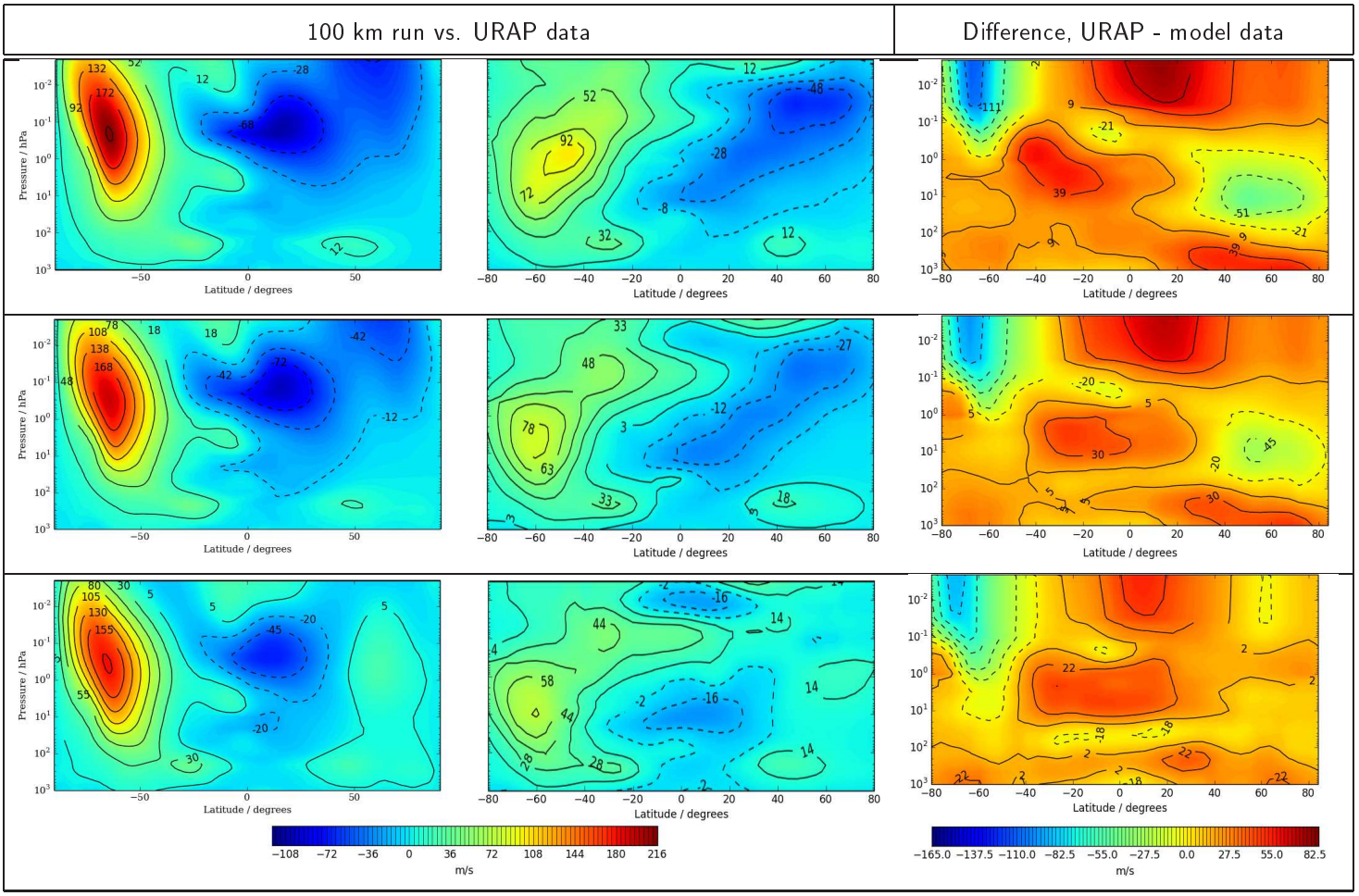

Figure 5.10: 100 km ceiling zonal mean U wind plots, July to September 1982, URAP observations July to September 1993. First column model data, second column URAP data, third column difference, first row July, second row August, third row September.

From July to August, a similar phenomenon is happening again, but this time from south to north (see Figure 5.10). Broad structures are represented, except for a mesospheric easterly, partially merged with the major southern westerly, which is absent in the model. I would speculate that, due to lack of gravity wave-induced deceleration, the westerly is adding to the speed of this major jet, rather than distributing it over the equator, as is observed by URAP. In July, the model's overestimation of wind speed is at its peak, representing a southern jet which is around 230% of the observed speed.

5.2.3 USSP off vs. USSP on

It was decided that comparison of the 100 km model with a previous run, done by Dr. Andrew Bushell with a 85 km ceiling, would be useful. This is because in Bushell's run, the non-orographic gravity wave scheme, Ultra Simple Spectral Parameterisation (USSP), is turned on, unlike in David Jackson's 100 km run. The USSP represents the forcing from a

continuous spectrum of gravity waves on the mean flow and assumes an isotropic and homogeneous wave source. It has been known to provide deceleration to the model jets, and thus representing the jets within realistic speeds.

Wave phenomena are crucial to understanding the dynamical structure of the atmosphere, for example in its temperature and zonal wind speeds. Waves, in particular gravity waves, mainly act as a momentum sink, sometimes as a source, to balance out Coriolis torque, and also affect radiative heat transfer (Brasseur & Solomon, 1986). Aforementioned sudden stratospheric warmings can also be affected, by topographically forced planetary waves. As detailed previously, planetary waves by their nature propagate upwards in westerly winds. Combined with the fact that there is significantly more land mass in the northern hemisphere, and that the northern hemisphere experiences more westerly winds in the stratosphere during the winter, this means that sudden stratospheric warmings are more readily observed in the winter months (Alexander & Shepherd, 2010). However, the presence or absence of cold volumes of air at the poles becomes the subject of most interest when considering the effects of the USSP gravity wave scheme.

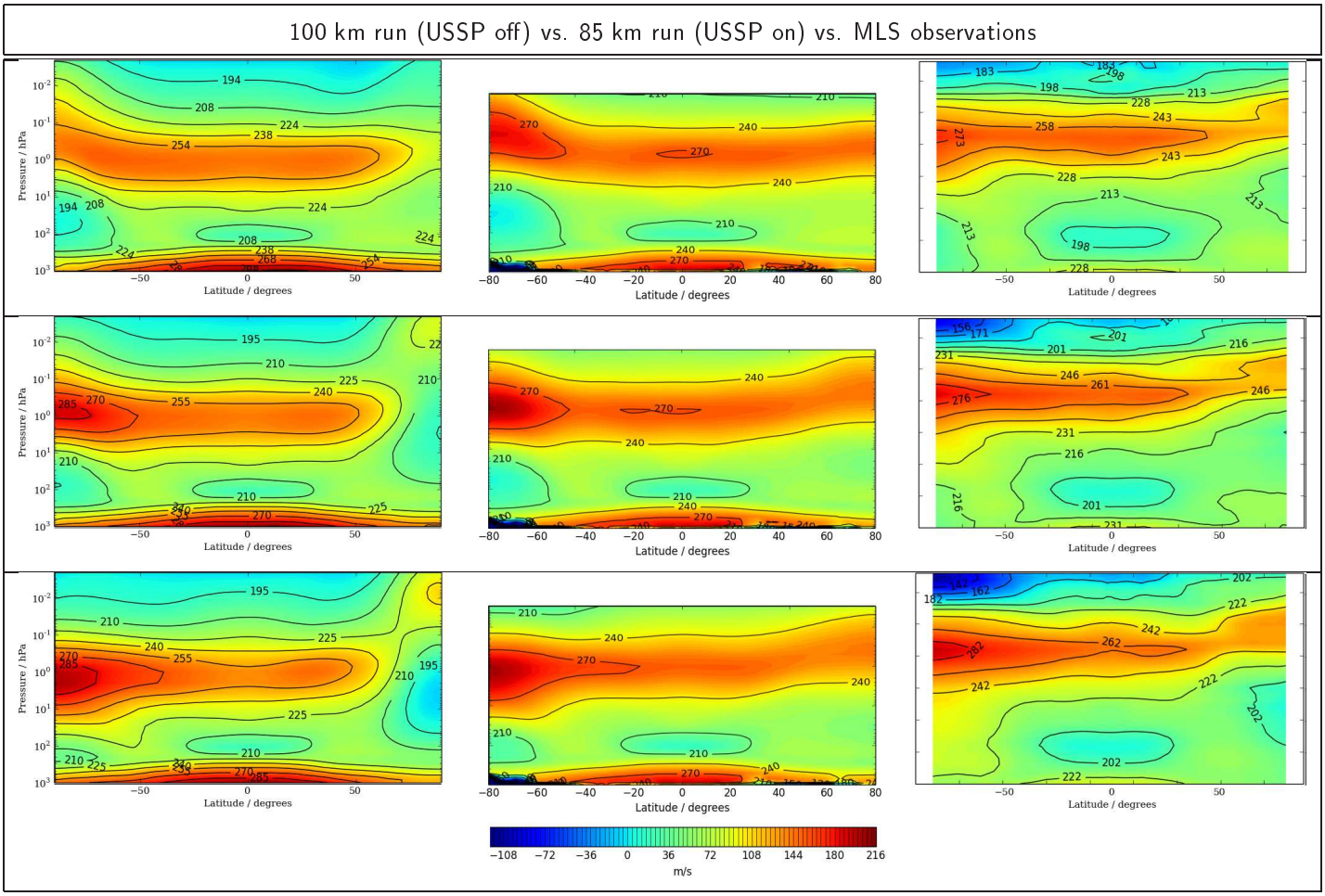

Figure 5.11: 100 km and 85 km ceiling zonal mean temperature plots, October to December 1981, MLS observations, October to December 2004. First column 100 km model data, second column 85 km model data, third column MLS data, first row October, second row November, third row December.

The aforementioned lowering of the latitude-spanning average warm air structure present in the 100 km run appears to be solved in the 85 km run, likely due to the presence of the USSP scheme in the latter (see Figure 5.11). The most significant deviation of the 85 km run from the 100 km run, and indeed the MLS observations, is the absence of a volume of cold air at the north pole from October to January. This minor "warm north pole problem" in the 85 km USSP run may be significant, however the yearly variability of temperatures may invalidate comparison of such minor structures.

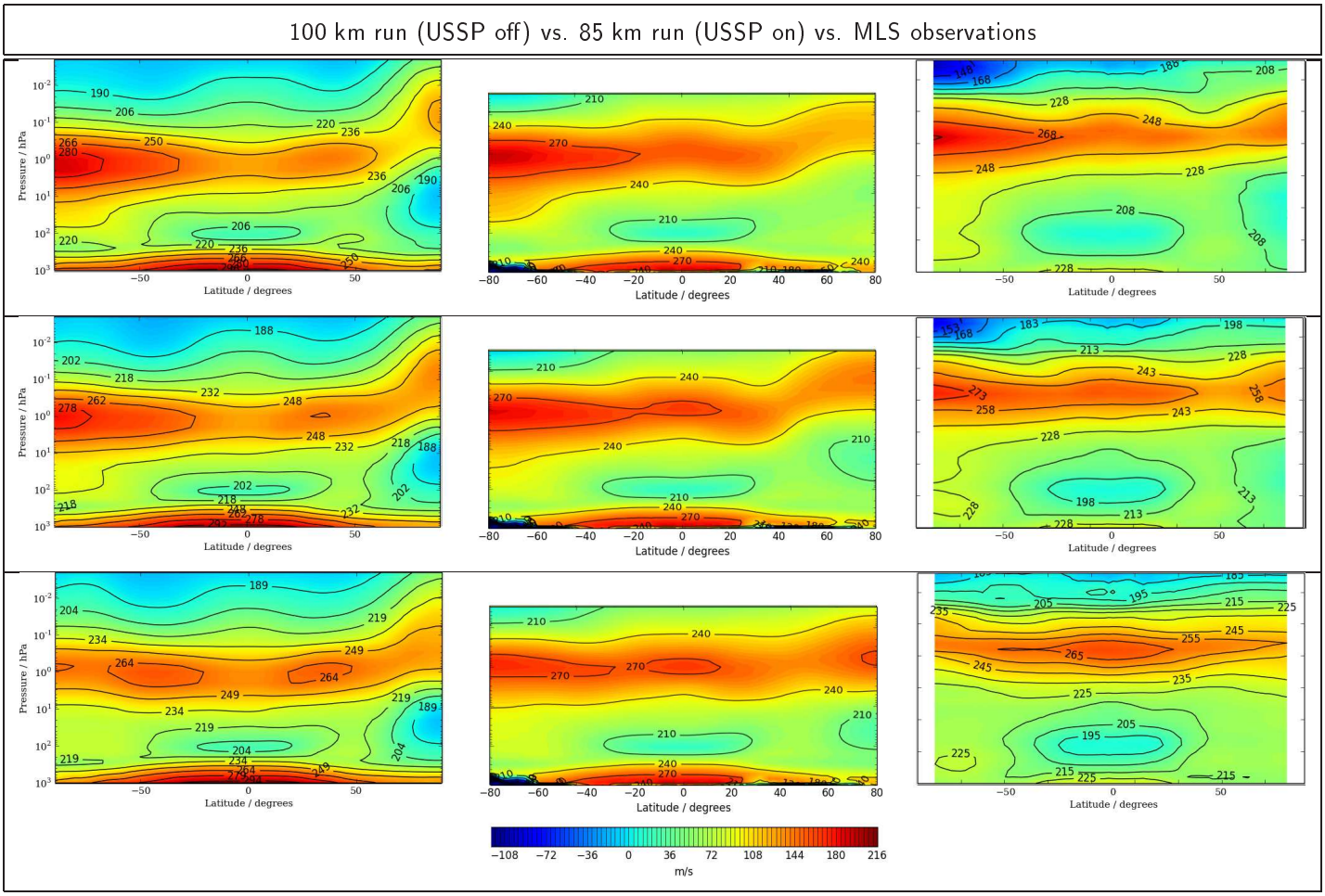

Figure 5.12: 100 km and 85 km ceiling zonal mean temperature plots, January to March 1982, MLS observations, January to March 2005. First column 100 km model data, second column 85 km model data, third column MLS data, first row January, second row February, third row March.

In Figure 5.12 we see the observed cold volume of air at northern latitudes become represented in the 85 km model, from February. Apart from this north pole volume, the two models are in broad agreement with each other and observations.

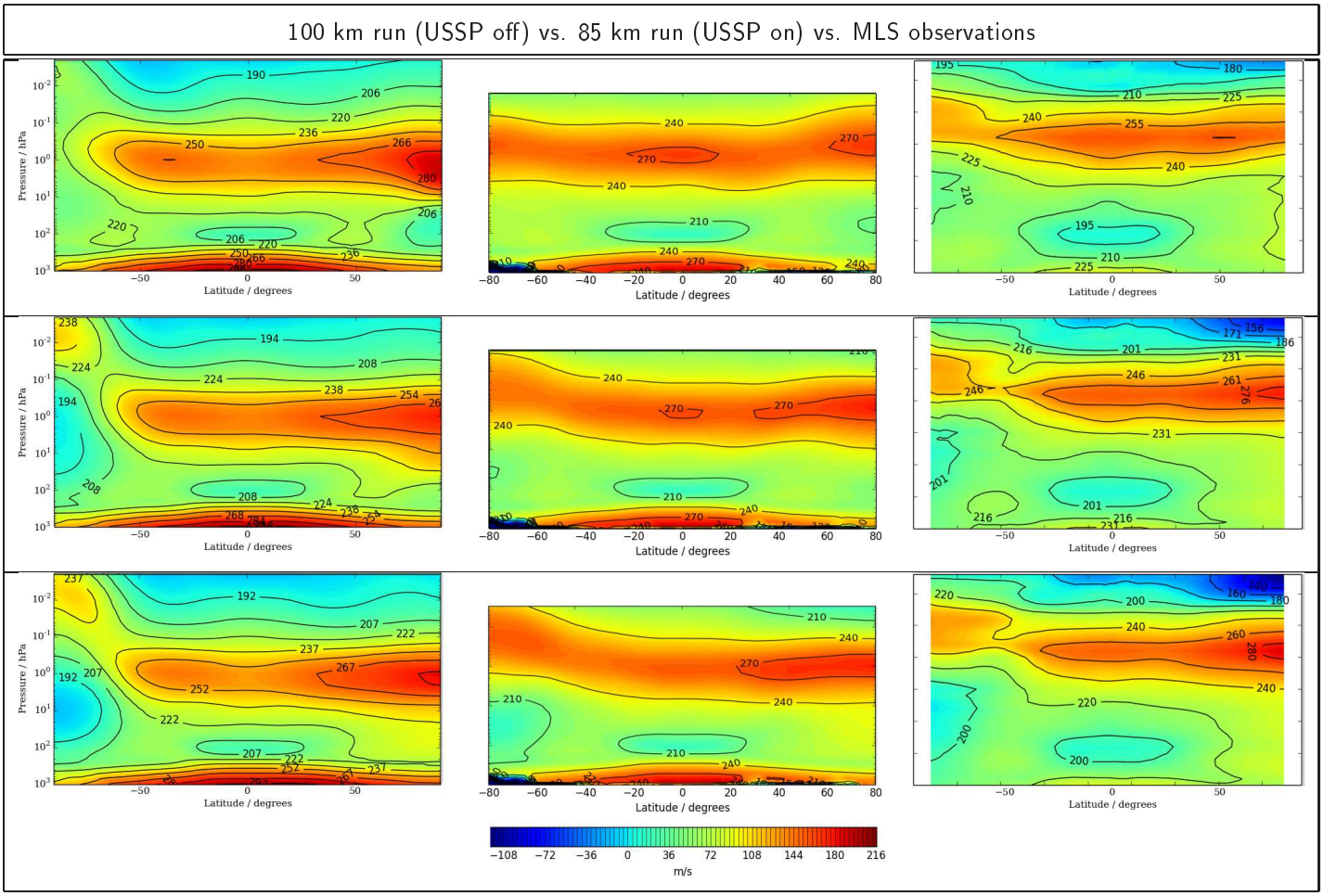

Figure 5.13: 100 km and 85 km ceiling zonal mean temperature plots, April to June 1982, MLS observations, April to June 2005. First column 100 km model data, second column 85 km model data, third column MLS data, first row April, second row May, third row June.

In Figure 5.13 we see that as the models begin to simulate the southern winter atmosphere, the 100 km run, lacking the USSP scheme, starts to underestimate the temperature of a cold volume of air at the south pole. On the other hand, the 100 km run does represent the southern structure of the major cross-latitude temperature belt well, in comparison to the 85 km run, where it is thicker and somewhat more simplistic than observed.

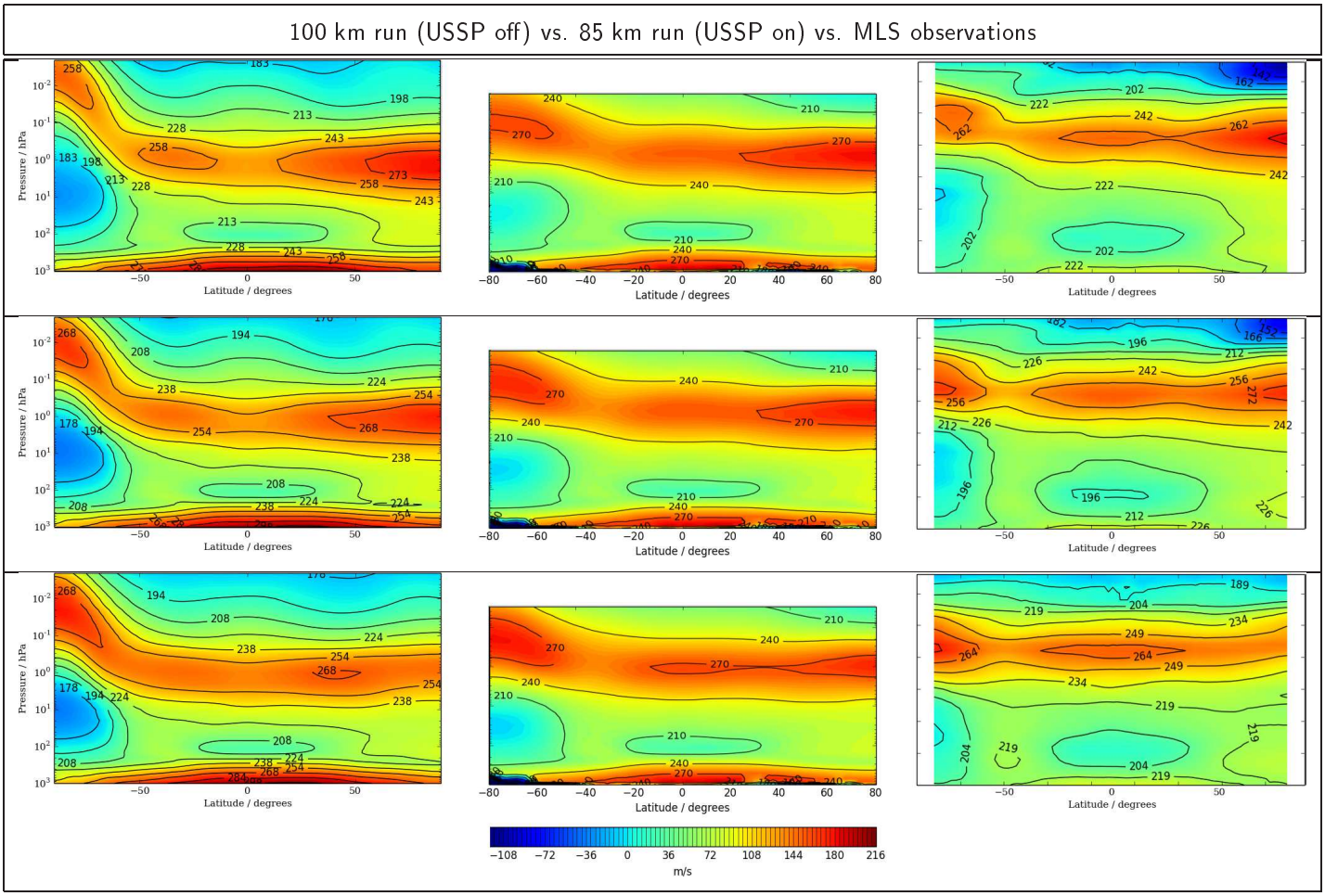

Figure 5.14: 100 km and 85 km ceiling zonal mean temperature plots, July to September 1982, MLS observations, July to September 2005. First column 100 km model data, second column 85 km model data, third column MLS data, first row July, second row August, third row September.

In Figure 5.14 the cold south pole problem in the 100 km run develops, with temperatures bcoming even lower than observed. As the cold south pole is represented in the 85 km run, the cross-latitudinal band is more accurately represented in the 85 km run for southern latitudes.

The 85 km run generally has a more realistic representation of zonal temperature, due to the absence of the underestimated temperature at the south pole, in the southern winter months (June to September) (see Figures 5.12 & 5.13). However, a minor caveat to this is that in December and January the 100 km run represents a volume of cold air which is observed, but which is absent in the 85 km run. In short, the 100 km run, with USSP turned off, has a "cold south pole problem", while the 85 km run, with USSP turned on, has a "warm north pole problem". The latter however, may not be outside the expected yearly variation in temperatures - further statistical analysis would ascertain its significance.

To further investigate the impact that the USSP scheme has, it is noteworthy to judge its impact on the winds themselves. Here (see Figures 5.14, 5.15, 5.16 & 5.17), the zonal u-winds are compared in the 100 km run (where the USSP scheme is off) and the 85 km run (where the USSP scheme is on), both on the same colour scale. Unfortunately, URAP observations cannot be used in this comparison because their dataset is defined in terms of pressure levels, and the 85 km run's wind output could only be acquired in terms of height, within the timespan of this project.

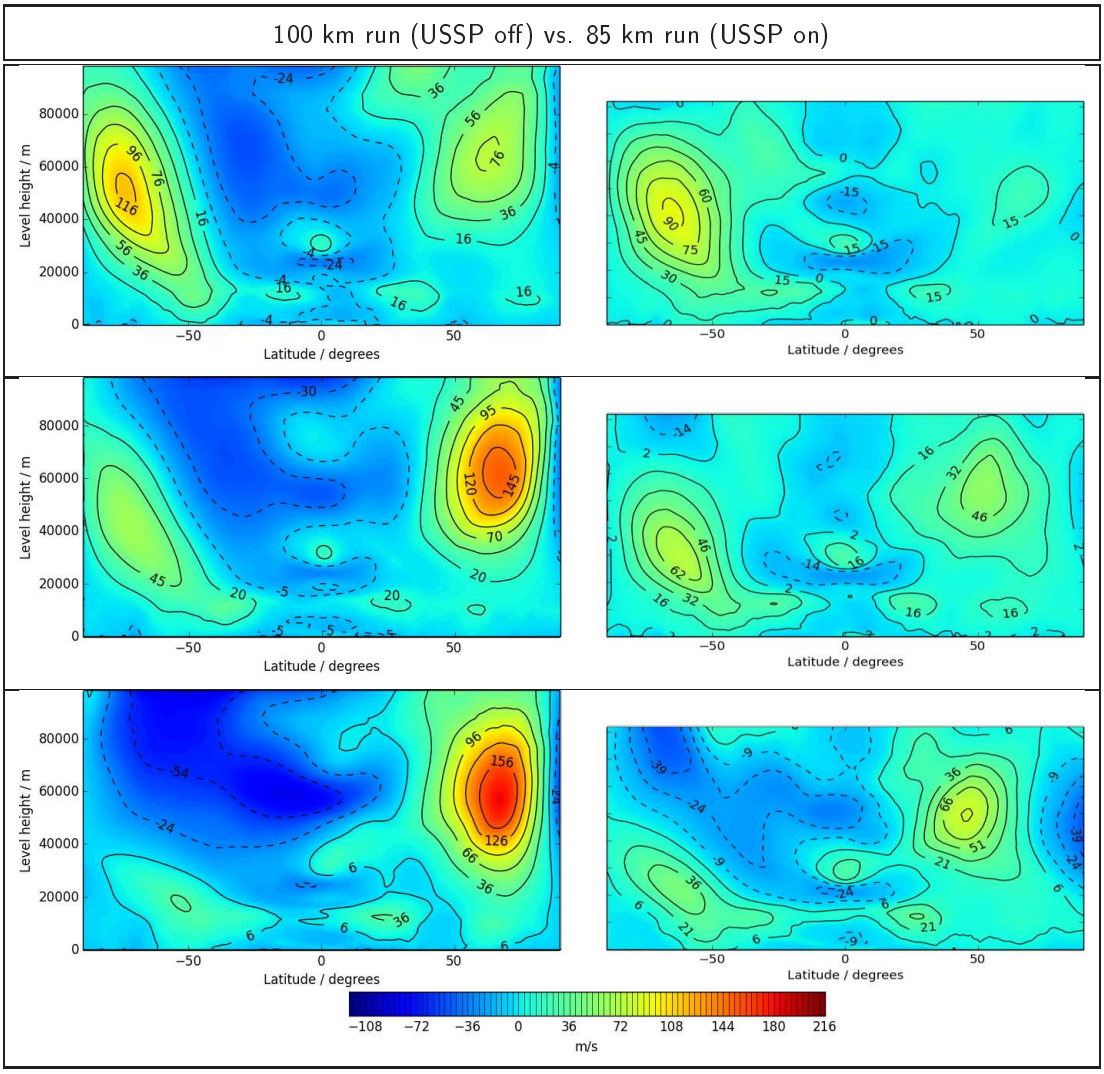

Figure 5.15: 100 km and 85 km ceiling zonal mean U wind plots, October to December 1981, URAP observations October to December 1991. First column 100 km model data, second column 85 km data, first row October, second row November, third row December

In Figure 5.15 we see the beneficial effect that the USSP scheme has on wind speeds, keeping them within a reasonable range. Another observation is the presence of equatorward tilting of wind structure at mesospheric altitudes in the 85 km run. The USSP scheme was noted for this effect in the UM in 2002, and it is considered a realistic product of the scheme (Scaife et al., 2002).

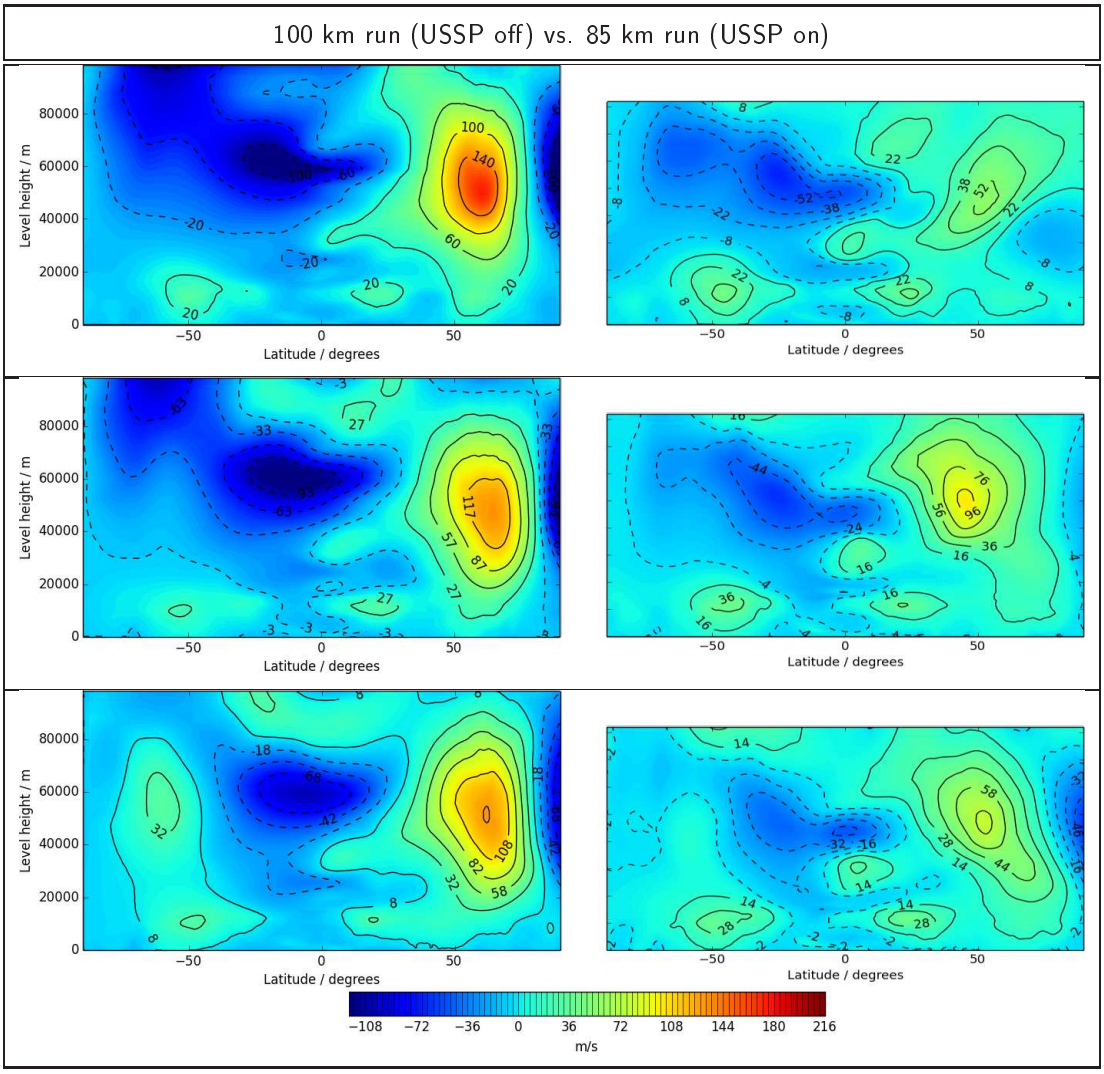

Figure 5.16: 100 km and 85 km ceiling zonal mean U wind plots, January to March 1982, URAP observations January to March 1992. First column 100 km model data, second column 85 km data, first row January, second row February, third row March

In Figure 5.16 we again see higher jet speeds in the 100 km run in the east and west directions, compared to the 85 km run, along with some equatorward tilting with altitude, albeit not as pronounced as in the 85 km run. Broadly, the respresentation of wind structure is similar in the two runs, but the USSP scheme in the 85 km run appears to represent finer jet structures.

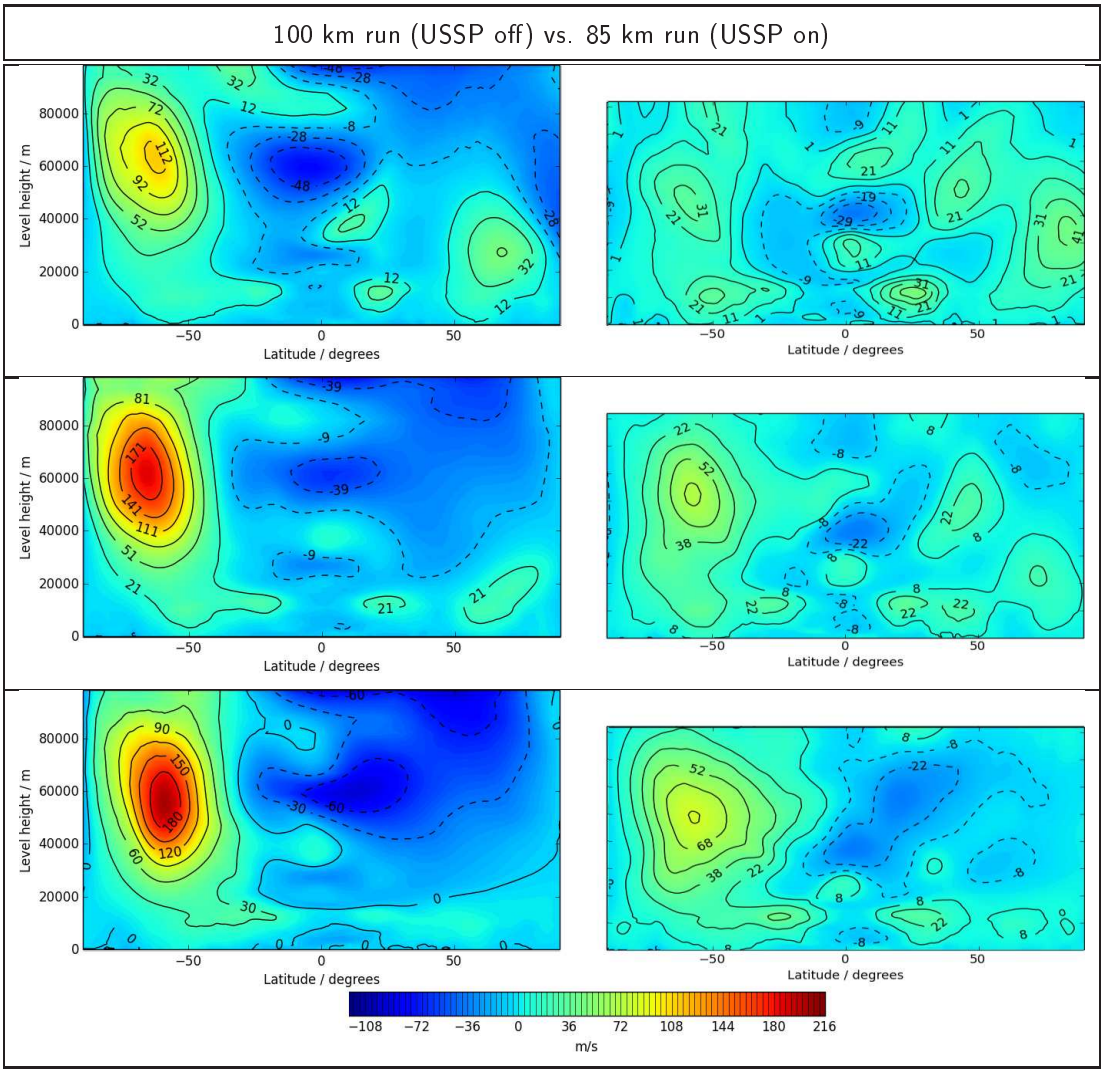

Figure 5.17: 100 km and 85 km ceiling zonal mean U wind plots, April to June 1982, URAP observations April to June 1992. First column 100 km model data, second column 85 km data, first row April, second row May, third row June

In April we see a major effect of the USSP scheme on the wind structure, with around 10 discernible jets in the east and west directions represented, compared with around 5 in the 100 km run in which the USSP scheme is absent (see figure 5.17). By June, the southern easterly in the 100 km run becomes exceptionally fast compared with the same jet in the 85 km run.

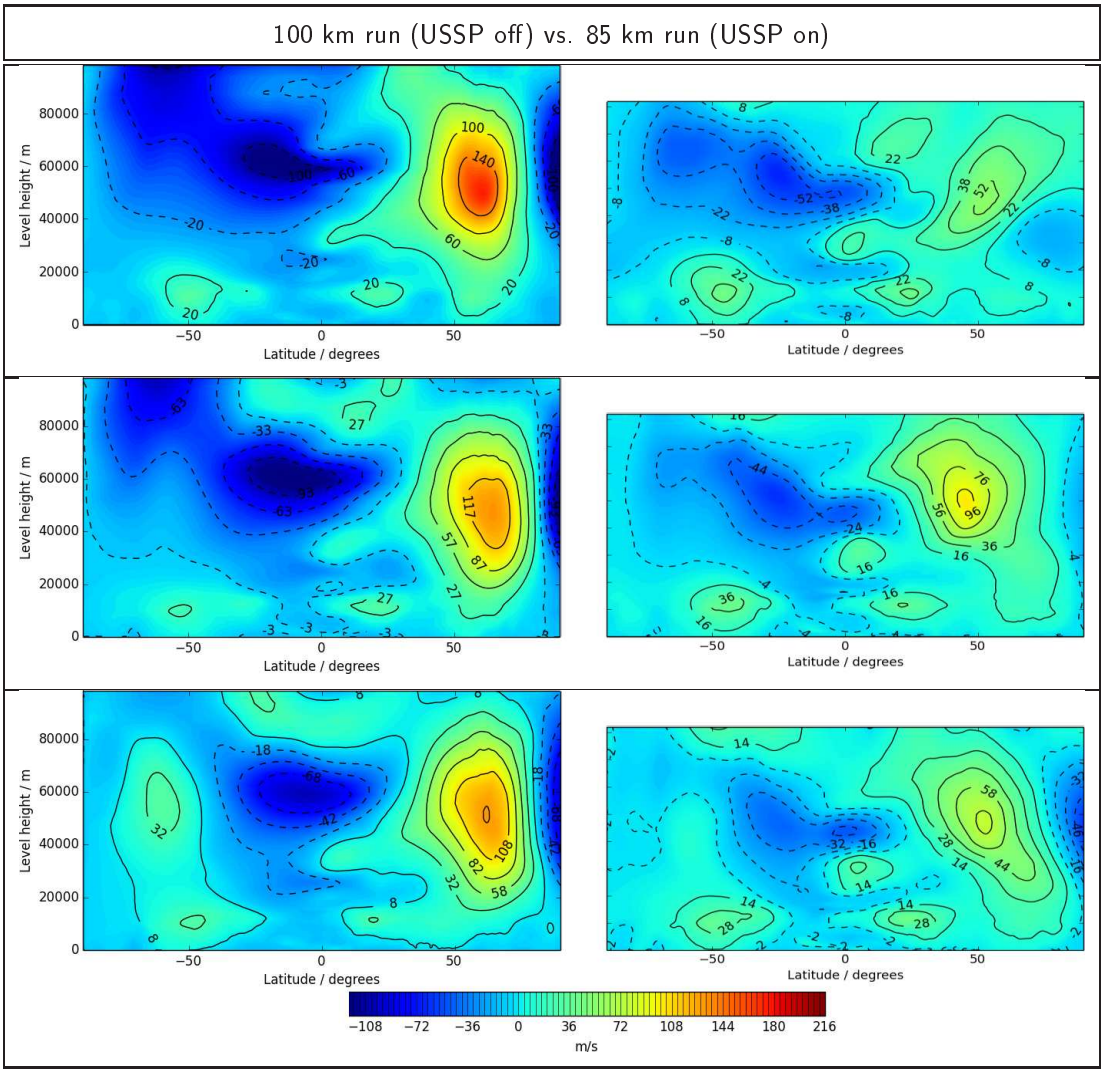

Figure 5.18: 100 km and 85 km ceiling zonal mean U wind plots, July to September 1982, URAP observations July to September 1992. First column 100 km model data, second column 85 km data, first row July, second row August, third row September

In Figure 5.18 we see a major speed difference in an equatorial westerly, which the USSP scheme appears to keep realistic, in comparison to the 100 km run. In summary, the USSP scheme reveals itself to be an effective component of the model in these comparisons (see Figures 5.15, 5.16, 5.17 & 5.18). The scheme preserves jet structures; in the 85 km run, the jets are small and many, compared with the 100 km run. The scheme also keeps the jet speeds in check; jets never reach speeds above 100 ms^{-1} in the 85 km run, broadly in keeping with observed speeds, while the 100 km run represents jets with speeds over 200 ms^{-1} . The scheme also reproduces realistic equatorward tilting of wind structures with altitude.

5.2 120 km ceiling

Here I assess the validity of the most stable 120 km ceiling run, which ran for 29.45 days. Unfortunately, due to the available outputs and the amount of time which would be taken by resubmitting the year-long 100 km run, the only variable I can compare is the zonal u-winds. The 100 km run's output only consists of monthly averages, while the 120 km run's output is in daily averages. Again, it isn't appropriate to compare the outputs with URAP winds, which are defined in terms of pressure and not height.

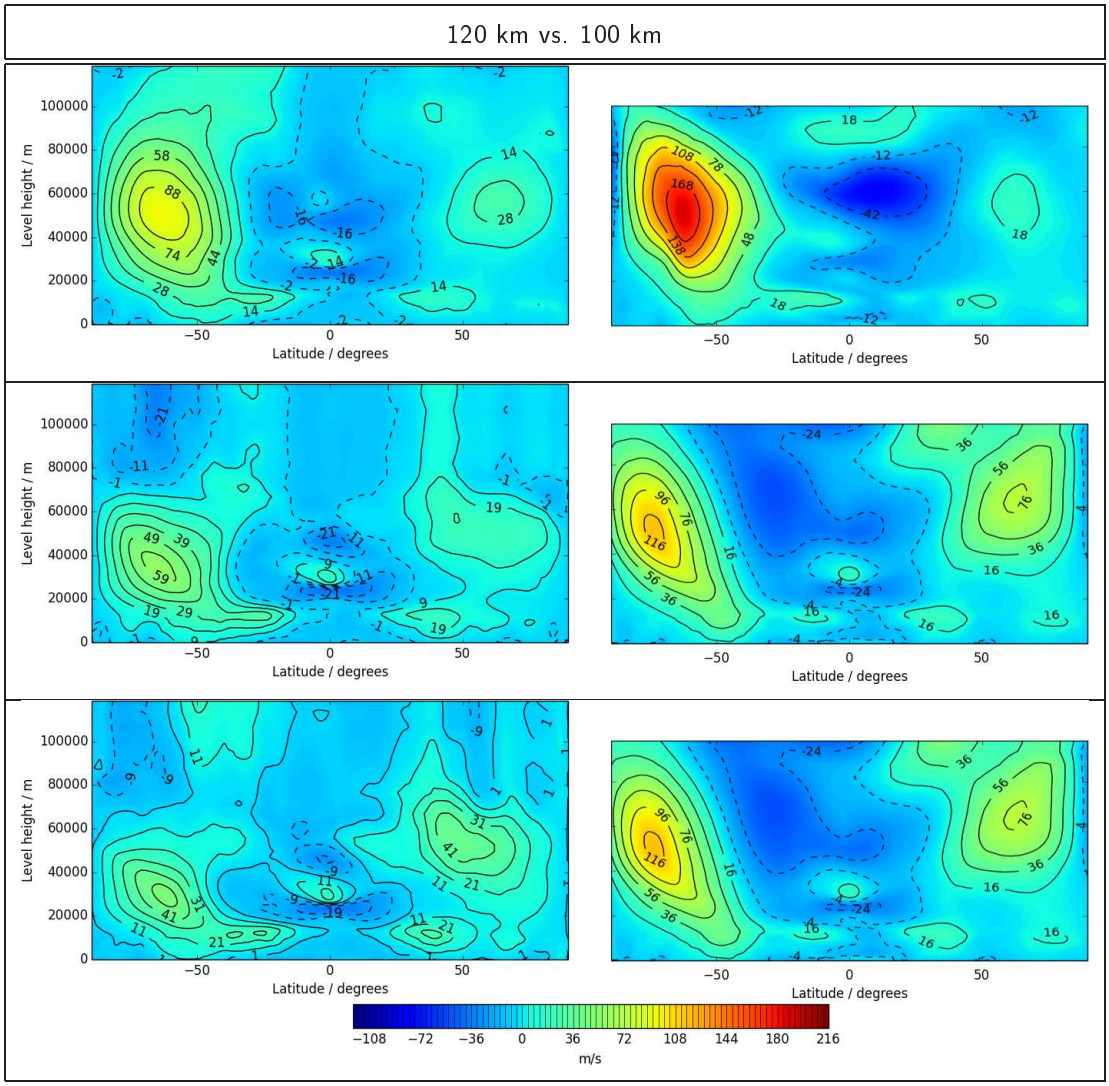

Figure 5.19: 120 km zonal daily mean (first column) vs. 100 km zonal monthly mean (second column) U-wind plots, 22 September vs. September (first row), 2 October vs. October (second row), 15 October vs. October (third row)

A noteworthy observation to make with the 120 km run is the development of vertical column structures in the winds, particularly at thermospheric altitudes (see Figure 5.18). There is a realistic slowing of winds through the month's simulation for altitudes below the thermosphere. However, there is unrealistic lack of wind structure in the thermosphere, where URAP data reveals to be an equatorial easterly, among other structures. It is worth noting that the USSP scheme is functioning in the 120 km run, so its effects could be too strong at mesospheric and thermospheric altitudes - its direct effects will now be explored.

Here (see Figure 5.20) I compare the effects of the 120 km run's USSP scheme with that of Bushell's 85 km run, specifically the zonal mean eastward force from USSP. While these forces are given in very small values, they were outputted in terms of metres per second per second. Therefore, considering their effects in terms of daily acceleration, they produce more significant values - as such, the limits of the colour bar are given in metres per second per day.

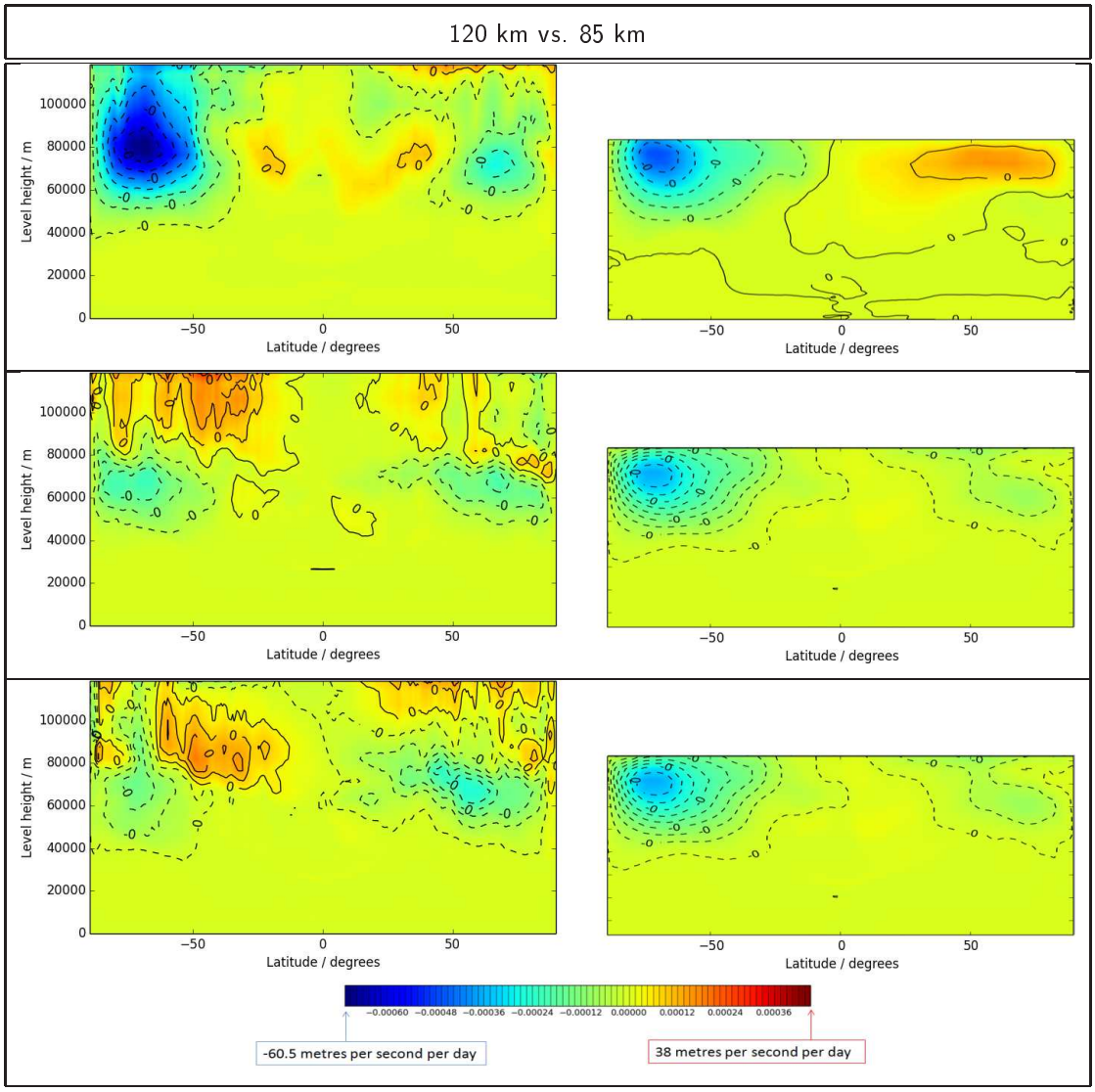

Figure 5.20: 120 km daily mean (first column) vs. 85 km monthly mean (second column) eastward spectral gravity wave force, 22 September vs. September (first row), 2 October vs. October (second row), 15 October vs. October (third row)

On the 22 September we see significantly greater westward acceleration from USSP in the mesosphere/thermosphere, at southern latitudes. This could be related to the aforementioned "cold pole problem", since it takes place at the same location and time of year (see Figure 5.20). On the 2 and 15 October, in the 120 km run's USSP we see eastward acceleration in a vertical column-type form, which is noteworthy because there is no eastward acceleration of any sort in the 85 km run's USSP. Also of interest is the appearance of some interaction between this eastward acceleration and the model ceiling - the strongest eastward acceleration is seen along the upper boundary at approximately -50° latitude. This may be due to the presence of easterly winds in the 120 km run whereas there are major westerlies in the 85 km run; the USSP scheme tends to produce

acceleration in the opposite direction to the wind.

Chapter 6

Conclusions and future work

The main results from my work are the following.

For ENDGame model runs with a 100 km ceiling, the USSP gravity wave scheme is not functioning. However, in David Jackson's year-long run, broad air temperature structure is well represented. There is a noted "cold pole problem" in the south pole in June to September. Consideration of the run's zonal u-winds reveal some good representation of structure, but a general overestimation of the jet's speeds and spacial volume, and a simplification of the jet's structures - a few large, slow jets are represented, instead of many small, slow ones. Comparison of the 100 km run's temperature and wind outputs with the same outputs from a previous 85 km run reveals benefits from the USSP gravity wave scheme, which is functioning in the latter. The USSP scheme reveals itself to be a solution to the "cold pole problem" present in the 100 km run's southern latitudes. However, in the 85 km run there is a noted problem which is minor relative to the south pole problem, namely a lack of representation of a cold north pole structure in December and January, which may or may not be statistically significant. The USSP scheme's effect on u-winds are significantly beneficial, preserving observed jet structure and keeping air speeds within a reasonable range, as well as reproducing a realistic equatorward titlting of jet forms.

When raising the lid to 120 km altitude, improved stability was noted when raising the off-centring parameter α to 0.99, and a spike in stability was noted when the vertical damping coefficient was set at 0.785. Such settings resulted in a run which is stable for 29.45 simulated days. Introduction of Rayleigh damping to the u- and v-winds produces a run which successfully submits and compiles but only computes the first timestep. Analysis of the 29.45 day 120 km run, which has a functioning USSP scheme, reveals more reasonable jet speeds than the 100 km run. However, there is the presence of unrealistic column structures to the winds. When considering the specific force that the USSP scheme exerts on the winds in the 120 km, one can see signficantly greater acceleration in the mesospheric south pole, which could be related to the aforementioned cold pole

problem, as well as erroneous westward acceleration, which seems to be interacting with the model ceiling itself.

Going forward, future avenues of work to be done include the following. The yearly variability of the MLS temperature observations could be quantified and the 85 km run's "warm north pole problem" could then be judged to be statistically significant or not. The run which implements Rayleigh damping could be debugged and its effect on the 120 km ceiling run's stability properly analysed. The discovered parameter values of 0.99 for α and 0.785 for the vertical damping coefficient will be useful for further stabilising 120 km ceiling runs. Also, the USSP scheme could be debugged for the 100 km ceiling setup, and its effect on stability and validity (especially the "cold south pole problem"), analysed.

Beyond the scope of this project, ENDGame's chemistry scheme is to be extended to the mesosphere and thermosphere. The ratio between O and N_2 influences the plasma density of the ionosphere's F region, for example, and so must be accurately modelled if an ionospheric model is to be coupled to ENDGame. Further ahead, non-LTE radiation schemes could be implemented above 120 km: calculating, for example, the solar heating of carbon dioxide in the near-infrared bands which demands consideration of non-LTE effects.

References

Ahrens, C. Donald., 2005, *Essentials of Meteorology*, Thomson Brooks/Cole.

Alexander, S. P., Shepherd, M. G., 2010, *Planetary wave activity in the polar lower stratosphere*, Atmos. Chem. Phys., Vol. 10, pp. 707–718.

Anderson, D., and Fuller-Rowell, T., 1999, *Space environment topics: the atmosphere*, Space Environment Center, Available at: http://www.swpc.noaa.gov/info/Iono.pdf (Accessed 26th October, 2014).

Andrews, D. G., Holton, J., Leovy, C., 1987, *Middle Atmosphere Dynamics*, Academic Press.

Akmaev, R. A., 2011, *Whole Atmosphere Modeling: Connecting Terrestrial and Space Weather*, Reviews of Geophysics, Vol. 49, pp. 4004-4034.

Akmaev, R. A., Wu, F., Fuller-Rowell, T. J., Wang, H., Iredell, M. D., 2010, *Midnight density and temperature maxima, and thermospheric dynamics in Whole Atmosphere Model simulations*, Journal of Geophysical Research, Vol. 115, Issue A8.

Bender, L., Burns, S.Z., David, L. (Producers), Guggenheim, D. (Director), & Gore, A. (Performer), 2006, *An inconvenient truth [Motion picture]*. United States: Lawrence Bender Productions & Participant Productions.

Bertaux, J. L. and Blamont, J. E., 1973, J. Geophys. Res., *Interpretation of Ogo 5 Lyman alpha measurements in the upper geocorona*, Vol. 78, pp. 80-91.

Bilitza, D, NASA, 2006, *COSPAR International Reference Atmosphere from NSSDC*, Available at: http://badc.nerc.ac.uk/view/badc.ne (Accessed 25 October, 2014).

Brasseur, G., Solomon, S., 1986, *Aeronomy of the Middle Atmosphere*, D. Reidel Publishing Co.

Burns, A., Emery, B., Foster, B., Lu, G., Maute, A., Qian, L., Richmond, A., Roble, R., Solomon, S., and Wang, W., 2011, *The NCAR TIE-GCM: Model Description, Development, and Validation*, High Altitude Observatory National Center for Atmospheric Research.

Darling, D. J., 2003, *The complete book of spaceflight: from Apollo 1 to zero gravity*, John Wiley & Sons.

Davies, T., Cullen, M. J. P., Malcolm, A. J., Mawson, M. H., Staniforth, A., White, A. A., and Wood, N., 2005, *A new dynamical core for the Met Office's global and regional modelling of the atmosphere*, Royal Meteorological Society, Vol. 608, pp. 1759–1782.

Deng, Y and Ridley, A. J., 2011, *Simulation of non-hydrostatic gravity wave propagation in the upper atmosphere*, Annales Geophysicae, Vol. 32, pp. 443-447.

Espy, P. J., Jones, G. O. L., Swenson, G. R., Tang, J., Taylor, M. J., 2004, *Seasonal variations of the gravity wave momentum flux in the Antarctic mesosphere and lower thermosphere*, Journal of Geophysical Research, Vol. 109, Issue D23.

Fomichev, V. I., V. P. Ogibalov, and S. R. Beagley, 2004, *Solar heating by the near-IR CO2 bands in the mesosphere*,

Geophys. Res. Lett., Vol. 31, Issue 21.

Fuller-Rowell, T. J., et al., 2008, *Impact of terrestrial weather on the upper atmosphere*, Geophys. Res. Lett., Vol. 35, Issue 9.

Goncharenko, L. P., Coster, A. J., Chau, J. L., and Valladares, C. E., 2010, *Impact of sudden stratospheric warmings on equatorial ionization anomaly*, Journal of Geophysical Research, Vol. 115, Issue A10.

Hunsucker, R. D., Hargreaves, J. K., 2003, *The high-latitude ionosphere and its effects on radio propagation*, Cambridge University Press.

Immel, T. J., Sagawa, E., England, S. L., Henderson, S. B., Hagan, M. E., Mende, S. B., Frey, H. U., Swenson, C. M., and Paxton, L. J., 2006, *Control of equatorial ionospheric morphology by atmospheric tides*, Geophysical Research Letters, Vol. 33, Issue 15.

Ineson, S., Scaife, A., Knight, J., Manners, J., Dunstone, N., Gray, L., Haigh, J., 2011, *Solar forcing of winter climate variability in the Northern Hemisphere, Nature Geoscience*, Vol. 4, pp. 753–757.

Jacobson, M. J., 2005 *Fundamentals of Atmospheric Modelling*, Cambridge University Press.

Jackson, D., 2012, *The Met Office Unified Model and its extension to the thermosphere*, UK-Germany National Astronomy Meeting.

Jin, H., Y. Miyoshi, H. Fujiwara, H. Shinagawa, K. Terada, N. Terada, M. Ishii, Y. Otsuka, and A. Saito, 2011, *Vertical connection from the tropospheric activities to the ionospheric longitudinal structure simulated by a new Earth's whole atmosphere-ionosphere coupled model*, J. Geophys. Res., Vol. 116, Issue A1.

Keil, M., 2007, *Paper 12.5: The Middle Atmosphere*, Met Office.

Kelley, Michael C., 1989, *The Earth's Ionosphere: Plasma Physics and Electrodynamics*, Academic Press.

Klobuchar, J. A., 1991, *Ionospheric Effects on GPS*, GPS World.

Marsh, D. R., Mills, M. J., Kinnison, D. E., Lamarque, J.-F., Calvo, N., and Polvani, L. M., 2013, *Climate Change from 1850 to 2005 Simulated in CESM1 (WACCM)*, J. Climate, Vol. 26, pp. 7372–7391.

McGraw-Hill, 1984, *Concise Encyclopedia of Science & Technology*, McGraw-Hill.

Nappo, Carmen J., 2002, *An Introduction to Atmospheric Gravity Waves*, Elsevier Science.

Norton, W. and Thuburn, J., 1999, *Sensitivity of mesospheric mean flow, planetary waves, and tides to strength of gravity wave drag*, Journal of Geophysical Research, Vol. 104, D24.

Pedatella, N. M., Forbes, J. M., 2010, *Evidence for stratosphere sudden warming ionosphere coupling due to vertically propagating tides*, Geophysical Research Letters, Vol. 37, Issue 11.

Roble, R. G., 2000, *On the feasibility of developing a global atmospheric model extending from the ground to the exosphere*, Geophys. Monogr. Ser., Vol. 123, pp. 53–67.

Rossby, C. G.; Collaborators, 1939, *Relation between variations in the intensity of the zonal circulation of the atmosphere and the displacements of the semi-permanent centers of action*, Journal of Marine Research, Vol. 2., p. 38-55.

Scaife, A. A., Butchart, N., Warner, C. D., Swinbank, R., 2002, *Impact of a Spectral Gravity Wave Parameterization on the Stratosphere in the Met Office Unified Model,* Journal of Atmospheric Science, Vol. 59, pp. 1473–1489.

Schwartz et al., 2008, *Validation of the Aura Microwave Limb Sounder temperature and geopotential height measurements,* Journal of Geophysical Research, Vol. 113, D15.

Sutton, E. K., 2008, *Effects of Solar Disturbances on the Thermosphere Densities and Winds from CHAMP and GRACE Satellite Accelerometer Data*, University of Colorado.

Swinbank, R., Ortland, D. A., 2003, *Compilation of Wind Data for the UARS Reference Atmosphere Project*, Journal of Geophysical Research, Vol. 108, Issue D19.

Tan, B., Liu, H.-L., Chu, X., 2012, *Studying 'cold pole' problem in WACCM and comparisons to lidar temperature morphology*, NCAR.

Tian, W., 2005, *A new coupled chemistry–climate model for the stratosphere: The importance of coupling for future O3-climate predictions*, Q. J. R. Meteorol. Soc., Vol. 131 , pp. 281–3.

Vallado, D. A., Finkleman, D., 2014, *A critical assessment of satellite drag and atmospheric density modelling*, Astra Astronautica, Vol. 95, p.p. 141-165.

Walters, D., Wood, N., Vosper, S., Milton, S., 2014, *ENDGame: A new dynamical core for seamless atmospheric prediction*, Met Office available at: http://www.metoffice.gov.uk/media/pdf/s/h/ENDGameGOVSci_v2.0.pdf.

Warner, C. D., McIntyre, M. E., 2001, *An Ultrasimple Spectral Parameterization for Nonorographic Gravity Waves*, J. Atmos. Sci., Vol. 58, pp. 1837–1857.

Waters, J. W. et al., 2006, *The Earth Observing System Microwave Limb Sounder (EOS MLS) on the Aura Satellite* Transactions on Geoscience and Remote Sensing, Vol. 44, No. 5.

Wood, N., Staniforth, A., White, A., Allen, T., Diamantakis, M., Gross, M., Melvin, T., Smith, C., Vosper, S., Zerroukat, M., Thuburn, J., 2013, *An inherently mass-conserving semi-implicit semi-Lagrangian discretization of the deep-atmosphere global non-hydrostatic equations,* Quarterly Journal of the Royal Meteorological Society, Vol. 140, pp. 1505–1520.